

# The Effect of Flame Structure on Soot Formation and Transport in Turbulent Nonpremixed Flames Using Direct Numerical Simulation

David O. Lignell<sup>a,\*</sup>, Jacqueline H. Chen<sup>a</sup>, Philip J. Smith<sup>b</sup>, Tianfeng F. Lu<sup>c</sup>, Chung K. Law<sup>c</sup>

<sup>a</sup>*Reacting Flow Research Department, Combustion Research Facility, Sandia National Laboratories, Livermore, CA 94551*

<sup>b</sup>*Department of Chemical Engineering, The University of Utah, Salt Lake City, UT 84098*

<sup>c</sup>*Department of Mechanical and Aerospace Engineering, Princeton University, Princeton, NJ 08540*

---

## Abstract

Direct numerical simulations of a two-dimensional, nonpremixed, sooting ethylene flame are performed to examine the effects of soot-flame interactions and transport in an unsteady configuration. A 15-step, 19-species (with 10 quasi-steady species) chemical mechanism was used for gas chemistry, with a two-moment, four-step, semi-empirical soot model. Flame curvature is shown to result in flames that move, relative to the fluid, either toward or away from rich soot formation regions, resulting in soot being essentially convected into or away from the flame. This relative motion of flame and soot results in a wide spread of soot in the mixture fraction coordinate. In regions where the center of curvature of the flame is in the fuel stream, the flame motion is towards the fuel and soot is located near the flame at high temperature, and hence has higher reaction rates and radiative heat fluxes. Soot-flame breakthrough is also observed in these regions. Fluid convection and flame displacement velocity relative to fluid convection are of similar magnitudes while thermophoretic diffusion is five-to-ten times lower. These results emphasize the importance of both unsteady and multidimensional effects on soot formation and transport in turbulent flames.

*Keywords:* soot, direct numerical simulation, nonpremixed flame, turbulent combustion

---

## 1. Introduction

Soot formation and growth in nonpremixed turbulent flames is an important process in practical combustion situations employing hydrocarbon fuels. Soot emission is known to have adverse health and environmental impacts, and its presence indicates incomplete combustion and reduced combustion efficiency. In addition, soot is the dominant source of radiative heat transfer in luminous flames and fires. Consequently, quantification of the physical phenomena of soot formation and transport in turbulent flames is important to obtain a fundamental understanding required for development of models for predictive calculations.

Turbulent flames are by definition unsteady and multi-dimensional, but the degree to which these two properties are important to a flame depends strongly on the reaction time and length scales of the flame. Hence steady, one-dimensional laminar flamelet assumptions [1], for example, have been used with much success for thin flames with fast reactions. Soot reaction and transport are different than those for gaseous species in two major ways. First, soot formation timescales are long compared to primary combustion reactions, and second, as a particulate phase, differential diffusion of soot is important. The long reaction

timescale of soot overlaps with diffusive and convective timescales resulting in potentially strong unsteady history effects. Differential diffusion effects may result in significant transport of soot in the mixture fraction coordinate, affecting the location of soot relative to the flame, and consequently soot temperature, which dictates reaction rates and radiative emission. Here the term differential diffusion is used to mean the difference between the Fickian diffusion of gaseous species and the thermophoretic diffusion mechanism of soot transport. The Fickian diffusion velocity of soot is practically zero due to the large molecular weight of soot.

Most detailed analyses of sooting flames have been confined to relatively simple flow configurations such as perfectly stirred reactors [2], one-dimensional freely propagating premixed flames [3], and laminar diffusion flames [4, 5, 6, 7], which have allowed detailed experimental investigation and comparison to computational models. These configurations are ideal for model development and validation. However, the vast majority of practical situations are turbulent. Experiments of turbulent sooting flames have provided mainly averaged quantities of soot and temperature fields, but have been unable to capture temporally and spatially resolved scalar fields. Due to computational costs, simulations of practical configurations have been confined to RANS and LES, which cannot resolve all time and length scales present in a flow, and must rely on subgrid models for closure of mean and filtered quantities

---

\*Corresponding author

Email address: doligne@sandia.gov (David O. Lignell)

representing unresolved turbulent transport.

In the present study we extend current capabilities of direct numerical simulation (DNS) with detailed chemistry to the study of a two-dimensional, nonpremixed, turbulent ethylene–air flame with soot formation. The purpose of the simulation is to observe and quantify effects of soot–flame interaction in a multidimensional, unsteady flow for which convection, diffusion, and reaction are all present.

Several previous studies have been performed that specifically examined the importance of flame structure and flow configuration on soot formation characteristics. Soot is formed on the fuel-rich side of diffusion flames, and the direction of the fluid convection relative to the flame, as well as flame shape and strain have a strong impact on the soot formation and growth. Smooke et al. [8, 6] have performed detailed experimental and computational studies of steady laminar co-flow diffusion flames. Shaddix et al. [7] compared pulsed normal and inverse co-flow ethylene diffusion flames. They note that while normal diffusion flames are a more natural configuration, inverse flames may have structures similar to those occurring in large-scale turbulent fires where an eddy may inject a pocket or *tongue* of air into a region of fuel. Kaplan et al. [9] performed simulations of unsteady pulsed methane–air diffusion flames showing large increases in peak soot concentrations over their steady counterparts due to increased soot residence time at favorable temperatures and stoichiometries in vortex structures.

In counterflow flames, increasing strain rate results in reduced levels of soot, mainly due to reduced residence time in reaction zones [10]. Stream doping/dilution (e.g. O<sub>2</sub>, CO<sub>2</sub> or N<sub>2</sub> addition) has been shown to affect soot levels both through temperature and chemical changes [11]. Several researchers have evaluated the effect on soot formation of altering the value of the stoichiometric mixture fraction through fuel dilution and oxygen enrichment in the fuel and oxidizer streams, respectively [10, 12, 13, 14, 15, 16]. For example, in ethylene flames the stoichiometric mixture fraction with pure fuel and air is 0.064. By systematically moving nitrogen from the air stream to the fuel stream, a stoichiometric mixture fraction of 0.78 can be obtained, with a constant adiabatic flame temperature [10].

For counterflow diffusion flames, shifting the stoichiometric mixture fraction can move the flame from one side of the stagnation plane to the other, hence changing the direction of the fluid convection through the flame. For flames that reside on the oxidizer side of the stagnation plane, convection transports soot away from the flame zone, minimizing the effects of oxidation and reducing the temperature of the peak soot concentrations; the converse is true for flames that reside on the fuel side of the stagnation plane, where convection transports soot toward the flame to higher temperatures and oxidation regions [15, 16].

Kang et al. [15] compared normal and inverse jet diffusion flames to counterflow opposed jet flames with vary-

ing stoichiometric mixture fraction to change the flame structure. They note the similarity of an inverse diffusion flame to the usual counterflow flame with the flame on the oxidizer side of the stagnation plane, and the similarity of a normal jet diffusion flame to a counterflow opposed jet flame with the flame on the fuel side of the stagnation plane. In this comparison, it is particularly interesting that, while counterflow flames require a change in the stream composition (stoichiometric mixture fraction) to change the flame structure, the two-dimensional diffusion flames can achieve similar flame structures through the hydrodynamic configuration. Kang et al. note that, in the normal diffusion flame, convective streamlines cross from the air side to the fuel side near the base of the flame (convecting soot away from the flame), while the opposite occurs at the top of the flame. They found that thermophoresis dominates soot diffusion and acts in the direction of convection near the base, and opposite of convection near the tip. multidimensional effects of curvature near the flame tip are also present, with thermophoresis tending to focus the soot particles into the fuel core.

In turbulent flames, which are inherently multidimensional and unsteady, we may expect similar behavior. That is, the structure of the soot–flame interaction will depend locally upon the direction of fluid convection relative to the flame, as well as on the flame shape. In the present paper, we use the insights gained from laminar flame structure to analyze turbulent soot formation and transport. Specifically, the effects of flame shape obtained from local curvature and fluid velocity normal to the flame are examined. The emphasis of this work is on flame structure and not turbulent mixing statistics. It is found that the differential diffusion of soot allows fluid convection relative to the flame to play a dominant role in the soot formation and growth process. The convection velocity relative to the flame is shown to depend on the flame curvature. These effects determine the location of soot in the mixture fraction coordinate, and hence the soot temperature, which has a strong impact on soot concentrations and radiative heat transfer.

## 2. Numerical Implementation and Models

### 2.1. DNS and Soot Modelling Approach

Direct numerical simulations fully resolve all continuum length and timescales of a reacting flow and are known to be computationally expensive as the cost of (3D) simulations scales approximately as  $Re^3$  [17]. Introduction of detailed combustion chemistry substantially increases the computational costs due to the number of additional scalars that must be transported (one for each chemical species) as well as the potential for decreased length and time scales, requiring finer grids and smaller timesteps. Inclusion of soot formation and growth further increases computational costs. Soot formation timescales are longer than gas combustion timescales, requiring longer run times.

Soot chemistry involves the formation and growth of large hydrocarbons and PAH species, notably benzene to pyrene (and on up), requiring transport of many chemical species. The relatively low diffusivity of soot also contributes to small spatial scales and increased resolution requirements. Soot exists as a particulate phase with an inherent particle size distribution, but a complete description of this distribution is not feasible in multidimensional, unsteady flows. In the present extension of DNS capabilities to sooting flames, a reduced description of the combustion chemistry was used to reduce the number of transported chemical species, and a semi-empirical soot model was applied in a manner similar to many approaches used in LES and RANS simulations. With the advantage of full resolution, the present simulation offers a unique look at the fundamental processes involved in soot-flame interactions.

The DNS code used is called S3D and was developed at Sandia National Laboratories. The code solves the fully compressible, three-dimensional reacting Navier-Stokes equations via finite difference approximations on a Cartesian grid. Equations for continuity, momentum, total energy, and chemical species mass fractions are solved in their conservative form. The ideal gas law equation of state is used throughout to compute the pressure from the density, temperature and composition. A fourth-order, six-stage explicit Runge-Kutta method is used for time advancement [18]. Spatial derivatives are evaluated using 8<sup>th</sup> order central difference approximations derived from Taylor series. A 10<sup>th</sup> order spatial filter is applied to remove high wavenumber content and reduce aliasing errors at each timestep [19]. All thermodynamic and transport properties are composition and temperature dependent and are evaluated using Chemkin III [20]. In the present simulation, mixture-averaged effective diffusivities were used with each species driven by its own mole fraction gradient (Fick-style). The mass fraction of the last chemical species, N<sub>2</sub> was computed to ensure conservation of mass, and thus the diffusion flux of N<sub>2</sub> implicitly enforces a null sum of species diffusion fluxes as required by continuity.

## 2.2. Gas Chemistry

A detailed mechanism [21] describing ethylene oxidation consisting of 70 species and 463 reactions was used to develop a reduced mechanism suitable to application in DNS. While the detailed mechanism is comprehensive and has been extensively validated, it is expected that not all the species and reactions are important within the parameter range covered in the current simulation. Furthermore, the vastly different time scales between the radicals and major species in the mechanism result in stiffness in the governing equations. Therefore, it is not computationally efficient to directly include the detailed chemistry in the simulation, and a reduced gas-phase mechanism was derived using a suite of recently developed systematic methods and strategies that facilitate the calculations [22, 23, 24, 25, 26]. Furthermore, in order to assure

the comprehensiveness of the reduced mechanism, which would be valid over the entire parameter range covered by the simulation, a set of reaction states were sampled from perfectly stirred reactors (PSR) and auto-ignition under atmospheric pressure, with equivalence ratios from 0.5 to 1.5 and ignition temperatures from 1000 to 1800K.

The first step of the reduction, namely skeletal reduction, is to eliminate unimportant species and reactions from the detailed mechanism. The soot model, described below, requires only gaseous species C<sub>2</sub>H<sub>2</sub>, O<sub>2</sub>, H<sub>2</sub>, and CO, which are retained in the final reduced mechanism. The method of directed relation graph (DRG) [22, 23] was first applied to eliminate species that are not important to any major species to be retained. This was followed by applying sensitivity analysis to species that appear to be moderately important, [24], which further eliminates the species that are truly not important to selected system parameters such as ignition delay, PSR extinction flow rate (residence time), laminar flame speeds, and the concentrations of selected important species including OH and C<sub>2</sub>H<sub>2</sub>. The resulting skeletal mechanism consists of 29 species, namely H<sub>2</sub>, H, O, O<sub>2</sub>, OH, H<sub>2</sub>O, HO<sub>2</sub>, H<sub>2</sub>O<sub>2</sub>, C, CH, CH<sub>2</sub>, CH<sub>2</sub><sup>\*</sup>, CH<sub>3</sub>, CH<sub>4</sub>, CO, CO<sub>2</sub>, HCO, CH<sub>2</sub>O, CH<sub>3</sub>O, C<sub>2</sub>H<sub>2</sub>, C<sub>2</sub>H<sub>3</sub>, C<sub>2</sub>H<sub>4</sub>, C<sub>2</sub>H<sub>5</sub>, C<sub>2</sub>H<sub>6</sub>, HCCO, CH<sub>2</sub>CO, CH<sub>2</sub>CHO, C<sub>3</sub>H<sub>6</sub>, and N<sub>2</sub>, and 167 elementary reactions.

Since species eliminated in the skeletal reduction are either slowly reacting, or are isolated and fast reacting, there are still fast-depleting radicals in the skeletal mechanism. Some of the radicals can be approximated to be in quasi steady state (QSS), such that their short time scales can be removed. Using computational singular perturbation [25], ten species, namely C, CH, CH<sub>2</sub>, CH<sub>2</sub><sup>\*</sup>, HCO, CH<sub>3</sub>O, C<sub>2</sub>H<sub>3</sub>, C<sub>2</sub>H<sub>5</sub>, HCCO, and CH<sub>2</sub>CHO, were found to be good QSS species within the entire parameter range of interest, resulting in a reduced mechanism consisting of 19 species, including N<sub>2</sub>, or equivalently 15 semi-global reaction steps. The concentrations of the QSSA species were then solved analytically using a method involving linearized QSS approximation with a QSS graph, [26]. Consequently, computational overhead is reduced and there are no nonlinear convergence issues, in contrast to traditional approaches requiring algebraic iterations.

The reduction is hereby complete. Computational efficiency was improved by the reduction in the number of species and the moderated stiffness. More specifically, the reduction in the species number alone yields a speedup factor of about three. The required time-step size of the reduced mechanism is about a factor of ten larger than that of the detailed mechanism, based on one-dimensional ignition tests consisting of a temporal-spatial ignition from a temperature spike on an open domain. The spatial grid size required by the reduced mechanism is about 1.5 times larger than that of the detailed mechanism. In two dimensions, the overall speedup of the reduced mechanism is about a factor of 65 (or 100 in 3D), which not only is significant but it also dictates the feasibility of a simulation.

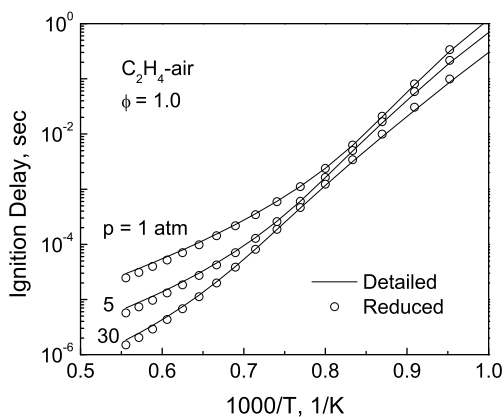


Figure 1: Ignition delay of  $C_2H_4$ -air mixture for auto-ignition with constant pressure as a function of initial temperature, calculated with detailed and reduced mechanisms, respectively.

The reduced mechanism was validated with homogeneous systems including PSR and auto-ignition, and diffusive systems including premixed and non-premixed ignition, and laminar flames. It is noted that although only non-premixed flames are studied in the present simulations, partially premixed regimes might exist due to the strong mixing processes, resulting in the need of comprehensive validation in terms of mixing. Furthermore, while the simulations are conducted at atmospheric pressure, the fidelity of the reduced mechanism under elevated pressures has also been assessed. Figure 1 compares the ignition delay time computed with the detailed and reduced mechanisms for the stoichiometric ethylene-air mixture. The agreement for the off-stoichiometric situations is similar since ignition delay is not sensitive to the equivalence ratio for homogeneous mixtures. The extinction residence time of PSR is shown in Fig. 2 for lean to rich mixtures. These two figures clearly show that the reduced mechanism accurately mimics the detailed mechanism for homogeneous ignition and extinction phenomena under a wide range of parameters. Figure 3 shows the calculated laminar flame speeds of premixed flames as a function of equivalence ratio. The worst case error is about 3 cm/sec, which is comparable to the uncertainty in many experimental measurements. The species concentrations in an opposed jet, non-premixed, ethylene-air flame are shown in Fig. 4. The temperature, major species, and minor species profiles all agree well, though moderate discrepancy is observed in  $C_2H_2$ . Based on these validation comparisons, confidence in the performance of the gas-phase mechanism for ethylene combustion under all conditions experienced in the DNS simulations is therefore adequately established. Furthermore, since the above validation covers a wide parameter range including pressure, the reduced mechanism developed is almost as comprehensive and accurate as the detailed one and its application can be readily extended

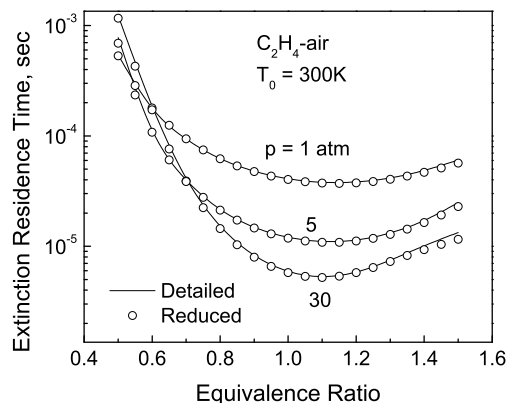


Figure 2: Extinction residence time of  $C_2H_4$ -air mixture in perfectly stirred reactors as a function of equivalence ratio, calculated with detailed and reduced mechanisms, respectively.

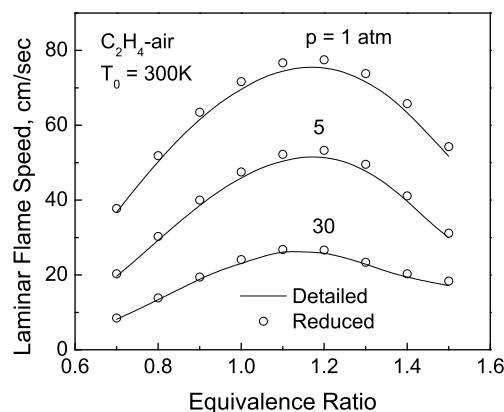


Figure 3: Laminar flame speeds of premixed  $C_2H_4$ -air mixtures as a function of equivalence ratio, calculated with detailed and reduced mechanisms, respectively.

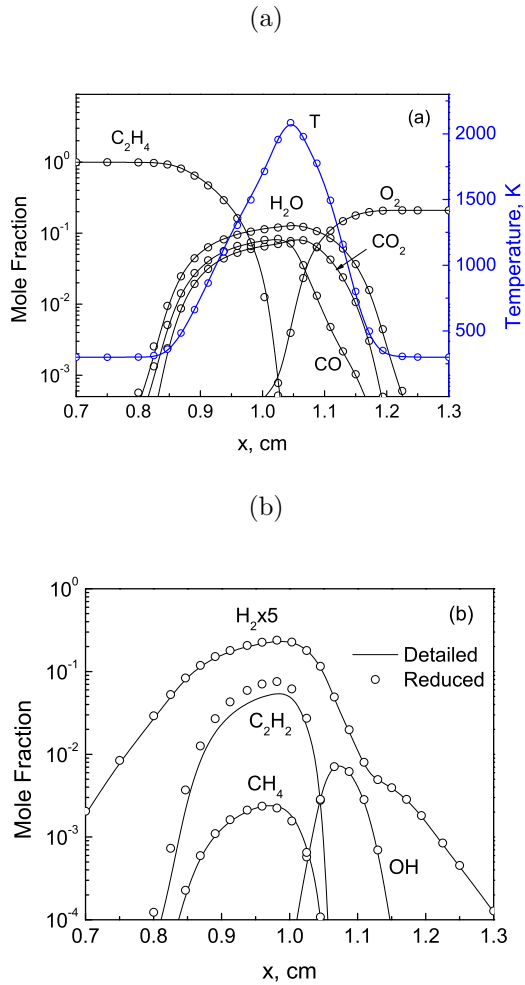


Figure 4: Profiles of a) temperature and major species, and b) minor species, for counterflow non-premixed flame with pure  $C_2H_4$  at  $x=0$  and air at  $x = 2$  under STP with a strain rate of  $100 \text{ s}^{-1}$ , calculated with detailed and reduced mechanisms, respectively.

to other applications.

While the detailed and reduced mechanisms have been shown to adequately describe ethylene combustion, the ability of the mechanism to predict general soot formation is not well characterized. Soot nucleation and growth, in the present soot model, however (discussed below), relies only on the acetylene concentration, which yields reasonable soot results when used with the current soot model. In applying the reduced mechanism, we are interested in comparing the concentration of the soot precursor and growth species acetylene. Since the reduced mechanism contains only C2 chemistry, the acetylene concentration is slightly over-predicted because higher hydrocarbon growth is not accessible as a sink. To further assess the extent of this effect, steady laminar flame calculations were performed at stoichiometric scalar dissipation rates of 1.3% and 13% of the extinction value of  $148 \text{ s}^{-1}$ . These values approximately bracket the mean stoichiometric dissipation rates encountered in the simulations. In both cases, the detailed mechanism had an acetylene concentration 20% lower than that of the reduced mechanism. Similar results were obtained using S3D with a relaxing one-dimensional diffusion flame initialized with a tanh profile in mixture fraction together with a flamelet solution as described below. Given the uncertainty in the detailed mechanism and the current soot models (both qualitative and quantitative) e.g. [3], an error in the soot precursor of up to 20% is not considered unacceptable.

### 2.3. Soot Model

The soot model implemented in S3D is that of Leung and Lindstedt [4], which has been used extensively in simulations of turbulent sooting jet flames. The model is a semi-empirical soot mechanism consisting of nucleation, growth, oxidation, and coagulation steps. The model is written in terms of the first two moments of the particle size distribution: soot mass fraction and number density. (The first two mass moments are number density  $n$  and soot mass per volume,  $\rho Y_{soot}$ ). These two quantities imply a monodispersed size distribution and are sufficient for defining a mean particle surface area needed for area-based surface growth and oxidation, where spherical particles are assumed. Soot is considered to be entirely carbon with a density of  $1850 \text{ kg/m}^3$ . Nucleation and surface growth occurs via acetylene with hydrogen evolved into the gas. The oxidation rate is written in terms of  $O_2$ , although it is known that OH oxidation is important. However, the oxidation rate expression is global, and so, to some extent, implicitly accounts for oxidation via other species (e.g. O, OH).

The soot chemistry is fully coupled to the gas-phase chemistry by adding the soot reaction source terms to the corresponding gas-phase species ( $C_2H_2$ ,  $CO$ ,  $O_2$ ,  $H_2$ ). Since the soot particles are small enough,  $O(50 \text{ nm})$ , and that the Stokes number is much smaller than unity, the soot particles are assumed to follow the gas velocity without any impact on the overall fluid momentum. With

soot included in the DNS simulation, the original governing equations of the gas-phase are not modified, except that the density appearing in the conservative form of the equations is taken to be the total density: gas plus soot mass per volume. In computing the system pressure, the gas-only density is used since soot exists at sub-ppm volume fractions, and has a negligible effect on the pressure. Soot formation is also coupled to the total energy equation through the heat capacity and internal energy of graphite for soot.

The transport equations for soot number density and mass fraction are, respectively,

$$\frac{\partial n}{\partial t} = -\nabla \cdot (n\vec{v}) - \nabla \cdot \vec{j}_n + S_n, \quad (1)$$

$$\frac{\partial(\rho Y_s)}{\partial t} = -\nabla \cdot (\rho Y_s \vec{v}) - \nabla \cdot \vec{j}_s + S_{Y_s}, \quad (2)$$

The diffusion flux was computed from

$$j_M = -\rho D_{p1} \nabla \left( \frac{1}{Le_s} \frac{M}{\rho} \right) - 0.556 M \frac{\nu}{T} \nabla T, \quad (3)$$

where  $M$  is either  $n$  or  $\rho Y_s$ . The first term represents Brownian diffusion, and the second term accounts for thermophoresis. This expression was derived similar to [27] from the general transport equation for the  $k^{th}$  particle size and applying the definition of the  $r^{th}$  soot mass-moment  $M_r = \sum_{k=1}^{\infty} m_1^r k^r n_k$ , (with  $m_k = k m_1$ ). Assuming the soot particle diffusivity in the free-molecular regime varies inversely as the square of the particle diameter as in [28],  $D_{p,k} \propto k^{-2/3}$ , so  $D_{p,k} = D_{p,1} k^{-2/3}$ . This results in fractional moments ( $M_{1/3}$  and  $M_{-2/3}$ ) in the diffusion flux of the transport equations (1), which are closed by logarithmic interpolation of  $M_0$  and  $M_1$ . Equation 3 results from assuming a unity Lewis number for particles of size  $k = 1$ ,  $Le_s = k^{2/3} = (\rho Y_s / n m_1)^{2/3}$ , where  $k$  is the number of carbons in the mean soot size defined by  $M_0$  and  $M_1$ . The first term in Eq. (3) is negligible [27], but is included for completeness. For example, nominal conditions of 1500 K and a volume fraction of 1 ppmv, and a number density of  $1 \times 10^{17} m^{-3}$ , gives  $Le_s \approx 9500$ . As implemented,  $Le_s$  is assumed to be locally constant, and therefore, taken outside the gradient.

#### 2.4. Radiation Model

Radiation is implemented using the optically thin assumption, with radiative emission from  $CH_4$ ,  $CO$ ,  $CO_2$ , and  $H_2O$ , with Planck mean absorption coefficients from [29]. The soot absorption coefficient is the same as that used in the RadCal package [30],

$$K_{soot} = 1864 f_v T, \quad (4)$$

where  $f_v$  is the soot volume fraction, and  $K_{soot}$  has units of inverse meters. Generally, sooting flames are known to be optically thick [6], with important impacts on temperatures and soot concentrations. Large, global flow scales,

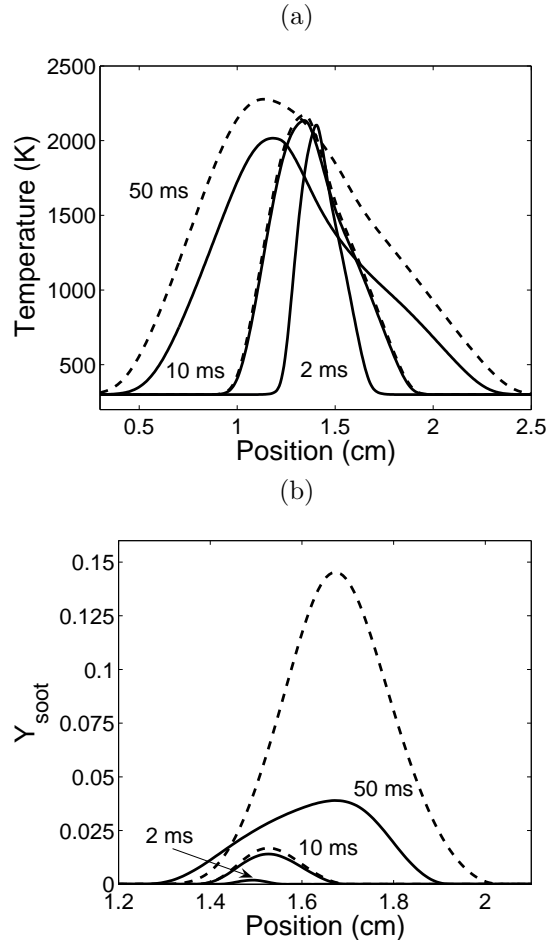


Figure 5: Temperature profiles (a), and soot mass fraction (b), at three times for the one-dimensional tests. Solid lines are the baseline case, and dashed lines are the baseline case with no radiative heat loss.

and their corresponding longer soot growth times necessitate the use of optically thick radiation models. However, the optically thin model is reasonable in the current DNS simulations, due to the small domain size (2 cm), and short run time (5 ms) associated with the local turbulent flame-soot interactions examined here. Two, one-dimensional tests were conducted of a relaxing, nonpremixed ethylene-air flame to test the radiative effects. The configuration and setup correspond to open boundaries with an initial tanh profile in mixture fraction initialized with a steady laminar flamelet, with a transition width of 0.1 cm. Figure 5 shows results of temperature and soot mass fraction profiles at three times, with and without radiation. The peak temperature differences are 0.3, 2 and 14% at 2, 10, and 50 ms, respectively. The peak soot mass fraction differences at the same times are 1.8, 19, and 270%. At 5 ms the soot mass fraction is 7% higher for the adiabatic case. Use of a more accurate, and more complex radiation model, with values lying between those of the adiabatic and optically thin models, is therefore not justified for the present simulation.

## 2.5. Configuration and Initial Conditions

The configuration chosen for study corresponds to a two-dimensional stripe of fuel surrounded by air, with a 2D isotropic turbulence field superimposed. Periodic boundary conditions are imposed in the direction of the fuel stripe (horizontal), and non-reflecting outflow boundary conditions are imposed in the other direction (vertical), resulting in a constant mean pressure. No mean velocity field is imposed. The intent of this configuration is to obtain a flame that is substantially influenced by a random, unsteady flow field, so that unsteady, multidimensional effects may be investigated. The configuration results in two flame surfaces on either side of the fuel stripe, increasing the amount of flame data, and resulting in a symmetric (except for the turbulent field) profile around the horizontal line splitting the fuel stripe. This configuration is inherently unsteady because of the decaying turbulence field and the lack of forcing of the velocity and composition fields. The case is a temporally-evolving simulation as opposed to a statistically stationary case, as might be observed in a non-premixed turbulent jet flame. This has the advantage of being less computationally expensive, as a smaller domain is required, allowed by the periodic boundaries. Likewise, the two-dimensional domain saves substantially on computational cost. It is emphasized that the purpose of the simulation is not to gather turbulent mixing statistics, but rather to examine the influence of an unsteady, multidimensional flame on soot formation and transport. To this end, the current simulation is believed to achieve this goal, with the results expected to carry over to more general cases of similar flame structure.

The fuel stripe consists of pure ethylene, 0.5 cm wide, surrounded by air (21% O<sub>2</sub>, 79% N<sub>2</sub>, by volume). The system pressure is 1 atm, and both stream temperatures are 300 K. The domain size is 2 cm in the direction of the fuel stripe and 3 cm in the transverse direction. The vertical dimension is chosen to keep the flame away from the boundaries of the domain. The total number of grid points is 960,000. A uniform grid size of 25 μm is used in both directions and is found to adequately resolve all chemical species and reaction rates. This was verified by conducting two-dimensional resolution tests in a temporal jet configuration with turbulent straining sufficient to induce extinction (which does not occur in the present simulations). Straining to extinction is conservative in that the smallest chemical species length scales (especially radical species) are observed at the point of extinction. No difference in species or velocity profiles were observed on grid sizes of 12 and 24 μm.

The initial, burning composition field is specified by setting the mixture fraction ( $\xi$ ) profile and using a steady laminar flamelet solution with composition and temperature given as functions of the mixture fraction. The mixture fraction represents the local mass fraction of gas originating in the fuel stream. A hyperbolic tangent function is used to transition between  $\xi = 0$  in the oxidizer and

$\xi = 1$  in the fuel, given by

$$\xi(y) = \frac{1}{2} \left( 1 + \tanh \left[ \frac{2}{\delta_\xi} (y - y_1) \right] \right) \cdot \frac{1}{2} \left( 1 + \tanh \left[ \frac{2}{\delta_\xi} (y - y_2) \right] \right), \quad (5)$$

where  $y_1$  and  $y_2$  are the centers of the transitions, and  $\delta$  is the width of the transition defined by

$$\delta = \frac{\xi_{max} - \xi_{min}}{\left| \frac{\partial \xi}{\partial y} \right|_{max}}. \quad (6)$$

The width,  $\delta_\xi$ , is 0.11 cm. Steady laminar flamelet solutions using a unity Lewis number assumption were computed to map the composition onto the domain through mixture fraction. The flamelet solutions were obtained by integrating the unsteady species flamelet equations to steady state via the equations [1]

$$\rho \frac{\partial Y_i}{\partial \tau} = \frac{\rho \chi}{2} \frac{\partial^2 Y_i}{\partial \xi^2} + \dot{m}_i'''. \quad (7)$$

The temperature was computed as  $T = T(h, Y_i)$ , where the enthalpy is known to be a linear function of mixture fraction for adiabatic, unity Le systems. The scalar dissipation rate in Eqn. 7 is defined as

$$\chi = 2D_\xi \left( \frac{\partial \xi}{\partial y} \right)^2. \quad (8)$$

Using the given tanh transition, the following equation couples the flamelet and physical domains

$$\chi = \frac{2D_\xi}{\delta_\xi^2} [1 - (2\xi - 1)^2]^2, \quad (9)$$

where  $D_\xi$  is the composition and temperature-dependent mixture fraction diffusivity (thermal diffusivity). The value of the transition width was about twice the extinction transition width and gave a scalar dissipation rate about one-third of the stoichiometric extinction dissipation rate of 156 s<sup>-1</sup>.

A turbulent velocity field was overlaid on the composition field in order to wrinkle the flame. The turbulence was initialized using an isotropic, homogeneous turbulent kinetic energy spectrum given by [31]

$$E(k) = \frac{32}{3} \sqrt{\frac{2}{\pi}} \frac{u'^2}{k_e} \left( \frac{k}{k_e} \right)^4 \exp \left[ -2 \left( \frac{k}{k_e} \right)^2 \right] \quad (10)$$

Here,  $k_e$  is the most energetic wave-number given by

$$k_e = \sqrt{\frac{4\epsilon}{10\nu u'^2}}. \quad (11)$$

The turbulence parameters were set by choosing  $u'$  and  $\epsilon$  such that the desired autocorrelation integral scale ( $L_{11}$ ) was obtained:

$$L_{11} = \frac{8}{3k_e} \sqrt{\frac{2}{\pi}}. \quad (12)$$

The turbulence field was filtered to within 1 cm of the open boundaries in order to keep the flow of the expanding flame from recirculating at the boundary. The autocorrelation integral scale and the most energetic length scales have values of 0.188, and 0.556 cm, respectively. The Reynolds number of the autocorrelation integral scale is 180, based on the air stream. The initial Kolmogorov length scale is 0.0076 cm giving 3 grid points across the Kolmogorov scale.

Table 1 summarizes the initial flame and turbulence parameters of the simulation, as well as estimates of important timescales. The turbulence timescale is defined as the ratio of  $L_{11}$  and  $u'$ , the flame dissipation timescale is defined as  $2/\chi_{st,ext}$ . The soot diffusion timescale is based on thermophoresis as  $\tau = \delta_\xi^2/0.554\nu$ , using the kinematic viscosity corresponding to products of  $\xi = 0.2$  at 1500 K, and the initial mixture fraction transition width. The soot reaction timescale corresponds to a nominal value based on global flow and mixing scales in e.g. jet flames (such as a jet exit velocity and a downstream location of peak soot). As such, this value is not an inherent reaction timescale but includes global, integral mixing effects. The present simulations are conducted to 5 ms, which is sufficient to examine the local soot-flame interactions under reasonable turbulence conditions noted below.

The timescales are of similar magnitudes except for the initial turbulence, which, however will increase with time. Note that the initial turbulence parameters are of the same order as those exiting a laboratory-scale turbulent jet. For example, Coppalle and Joyeux [32] studied a turbulent flame with an exit velocity of 30 m/s (a  $u'$  of 5% of the exit is typical) and an initial jet diameter of 4 mm. Hu et al. [33] studied similar flames and cited soot layers down to 1 mm and integral scales of approximately 5 mm. So, the values in Table 1 are reasonable and should allow the DNS results to be relevant qualitatively to practical situations.

### 3. Flame Analysis

The location of peak soot concentration and soot transport, relative to a flame zone are important since they dictate the soot temperature, and hence reactivity and radiative properties. This relative motion results from the combined effects of fluid convection, gaseous species diffusion, and thermophoretic diffusion of soot. To quantify these effects, we define the flame location as the position of the stoichiometric iso-surface of mixture fraction. Mixture fraction is computed from the local DNS composition fields using Bilger's definition [34]. Since soot mainly follows pathlines of the fluid convection (with an additional thermophoretic diffusion component), the motion of the stoichiometric iso-surface of mixture fraction relative to the local fluid convection gives a sense of whether soot will be convected into or away from a flame zone. Gibson [35] and Pope [36] derived the expression for the velocity of a constant-property scalar iso-surface relative to the local

fluid motion. For variable properties, the relative velocity is

$$\mathbf{v}_\xi = -\frac{\nabla \cdot (\rho D_\xi \nabla \xi)}{\rho |\nabla \xi|} \mathbf{n}, \quad (13)$$

where  $D_\xi$  is the mixture fraction diffusivity and  $\rho$  is the density. In this equation, the surface velocity relative to convection is due to diffusion in the direction of the surface normal, defined by

$$\mathbf{n} = \frac{\nabla \xi}{|\nabla \xi|}, \quad (14)$$

where the normal points towards the fuel stream. Henceforth,  $v_\xi$  will be referred to as the flame displacement velocity. For  $v_\xi > 0$  the flame is moving toward the fuel stream and for  $v_\xi < 0$  the flame is moving toward the air stream. The direction of convection across the flame is  $v_{fc} = -v_\xi$ . Thus, for negative  $v_\xi$  the fluid is convecting across the flame from the air side to the fuel side, and we expect soot to be convected away from the flame zone. This situation is analogous to the canonical fuel-air counterflow configuration.

Equation 13 contains multidimensional effects that can be expanded in terms of flame-coordinates as done by Echehki and Chen [37] who applied a similar analysis to premixed flames. By applying the chain rule of differentiation to  $|\nabla \xi| = \mathbf{n} \cdot \nabla \xi$  in Eq. 13, and introducing the operator  $\frac{\partial}{\partial \eta} = \mathbf{n} \cdot \nabla$ , and so noting that  $|\nabla \xi| = \frac{\partial \xi}{\partial \eta}$ , we obtain

$$v_\xi = -D_\xi \nabla \cdot \mathbf{n} - \frac{1}{\rho |\nabla \xi|} \frac{\partial}{\partial \eta} \left( \rho D_\xi \frac{\partial \xi}{\partial \eta} \right). \quad (15)$$

Here,  $\eta$  is the flame-normal coordinate in the direction  $\mathbf{n}$ .

The first term represents the contribution due to iso-surface curvature, where  $\nabla \cdot \mathbf{n}$  is the curvature of the iso-surface. With this definition, curvature is taken to be positive when the center of curvature is on the oxidizer side. The second term in Eq. 15 is relative flame motion due to diffusion in the direction normal to the flame. The normal diffusion contribution to the flame displacement velocity can be written in terms of the scalar dissipation rate defined as  $\chi = 2D_\xi |\nabla \xi|^2$ . This is done by rearranging the definition of  $\chi$  to give  $|\nabla \xi| = \sqrt{\chi/2D_\xi}$ , substituting this into  $|\nabla \xi|$  and  $\frac{\partial \xi}{\partial \eta}$  in Eq. 15, and simplifying, to give

$$v_\xi = -D_\xi \nabla \cdot \mathbf{n} - \frac{D_\xi}{2} \frac{\partial}{\partial \eta} \ln(\rho^2 D_\xi \chi/2). \quad (16)$$

Hence, the flame displacement velocity is made up of a curvature component and a normal diffusion, or scalar dissipation rate component.

This type of analysis, in which the flame surface motion is studied, has been extensively applied to premixed combustion in the development and use of the G-equation [38]. Application to nonpremixed combustion is less common, and has been mainly used in the development of flame surface area models [39, 40].

Figure 6 shows the schematic of a hypothetical, strained and curved nonpremixed flame. The solid line represents

Table 1: Simulation parameters and timescales.

Parameter		Parameter		Timescale (ms)	
$L_x$ (cm)	2	$\delta_\xi$ (cm)	0.11	Turbulence	1.25
$L_y$ (cm)	3	# cells	960,000	Soot reaction	10
$L_{11}$ (cm)	0.188	# timesteps	325,000	Soot diffusion	6
$u'$ (cm/s)	150	Run time (ms)	5	Flame dissipation (ms)	13
$H_\xi$ (cm)	0.5	Sim. Cost. (cpuh)	32,500		

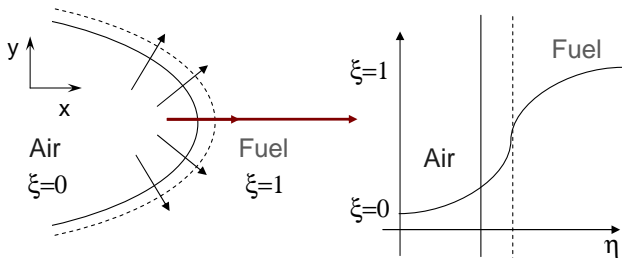


Figure 6: Schematic of a curved diffusion flame. The solid line represents the stoichiometric surface and the dashed line the  $\xi = 0.5$  surface.

the flame surface and the dashed line is the location of  $\xi = 0.5$ , nominally the inflection point in the profile normal to the flame. The right half of the figure shows the mixture fraction profile along the bold center normal. The two halves of the figure illustrate the two terms in Eq. 15 and show that either term may be positive or negative depending on the direction of curvature and the location of the flame. Generally, we may expect the normal diffusion term to contribute to a negative flame displacement velocity since the flame resides on the lean side of the inflection point (where the second derivative of  $\xi$  is positive with respect to  $\eta$ ). The curvature term competes with, or complements the normal diffusion term. In the figure, curvature is positive and contributes to a negative flame displacement velocity, so that normal diffusion and curvature tend to move the flame to the left toward the air stream. However, if we reverse the curvature, at some point it will be sufficiently negative to overcome the normal diffusion term, and the flame will move to the right toward the fuel stream. Qualitatively, we can consider the rate of change of mixture fraction between the dashed and solid lines as  $j_s A_s - j_d A_d$ . The flux and areas are higher at the dashed line than the solid line (resulting in a net loss of  $\xi$  and motion to the left), but as we reduce curvature, the ratio of the areas of the solid to dashed lines increases so that, for constant fluxes, there can be a net gain of  $\xi$ , with motion of the iso-surfaces to the right.

We can see that flame wrinkling is a clear mechanism by which soot (essentially convected with the flow) is dif-

ferentially transported towards or away from the flame. Convection through the flame implies motion in the mixture fraction coordinate, to which temperature and species concentrations are primarily tied. Thermophoretic diffusion will transports soot down temperature gradients, away from the flame zone toward the fuel, so that, from the point of view of the soot, we could consider the sum of soot convection and diffusion, rather than just soot convection. The main observation, however, is that turbulent motions themselves can alter the direction of flow through a flame, which can impact soot concentrations.

In the following sections, results are also presented of quantities along directions normal to the flame at a given instant in time. Flame normal directions are defined as above, and computed as follows. Mixture fraction normal vectors were computed at all grid points and interpolated to all intersections of the stoichiometric mixture fraction with the grid lines. Points in the domain were then computed at regular distances (about equal to the grid spacing) along the normal direction, and all field quantities were linearly interpolated to these points. Normals were cropped at any point where the mixture fraction profile became non-monotonic.

## 4. Results

### 4.1. Overview and Observations

The simulation was computed to a time of 5 ms. Figure 7 shows instantaneous snapshots of temperature, acetylene mass fraction and soot mass fraction at times of 1.25, 2.5, 3.75, and 5 ms. In each series, only the interesting portion of the domain is shown. The soot mass fraction range shown is 0 to 0.003 for clarity, but the peak values are 0.0024, 0.008, 0.013, 0.022 (or about 0.3, 1.0, 1.7, 2.9 ppmv) in time. As time progresses, the flame is wrinkled by the turbulence resulting in enhanced mixing of fuel and oxidizer as the flame expands. In each figure, two isocontours of mixture fraction are shown corresponding to the stoichiometric isocontour ( $\xi = 0.064$ ), and the approximate peak in the soot precursor/growth species acetylene ( $\xi = 0.2$ ).

Of particular interest in these progressions is the motion of the stoichiometric contour. In several regions, especially those with positive curvature, the flame is observed to move away from the fuel side, reducing the curvature.

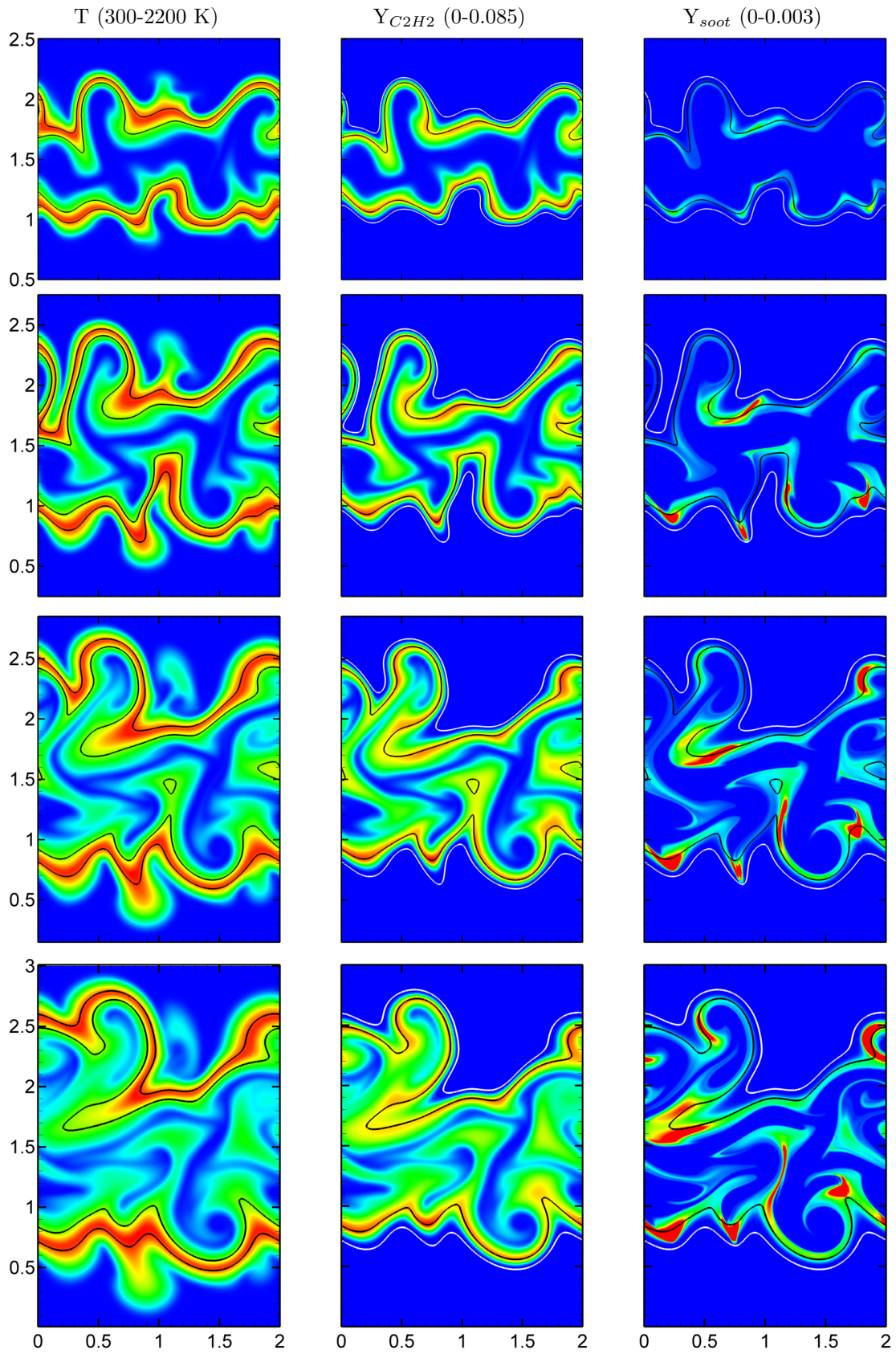


Figure 7: Vertical time series with indicated ranges (red is high). Times are 1.25, 2.5, 3.75, 5.0 ms. Contours at  $\xi = 0.064, 0.2$  (white for clarity only).

In these regions, the curvature and normal diffusion components of the flame displacement velocity in Eq. 15 are expected to have the same sign, resulting in enhanced motion. In regions of negative curvature, the curvature contribution results in displacement of the flame towards the fuel, while the effect of normal diffusion is to displace the flame towards the oxidizer. This results in a partial cancellation of flame motion effects, and a more stagnant flame surface.

For the range of unsteady strain rates imposed by the initial velocity spectrum, local extinction is negligible, and gaseous combustion timescales are small compared to flow timescales. The temperature peak is concentrated around the stoichiometric mixture fraction isocontour, while the acetylene peak follows the  $\xi = 0.2$  isocontour. The spacing of the mixture fraction isocontours is an indication of the local scalar dissipation rate. Acetylene concentrations tend to be lower in regions of higher scalar dissipation rate. Peak soot concentrations are not observed to be as tightly bound to the indicated isocontours as temperature and acetylene mass fraction are. Initially, soot levels are confined near the  $\xi = 0.2$  mixture fraction isocontour, while at later times, high soot levels are observed in richer (and leaner) regions. In particular, we observe regions in Figure 7 in which the motion of the positively curved flame essentially leaves the soot behind. Along the flame, it is clear that the soot concentration is not homogeneous, but that the peak soot levels tend to occur in regions of large negative flame curvature.

Figure 8 shows fields of soot number density, scalar dissipation rate, OH mass fraction, and soot reaction rates of nucleation, growth and oxidation at a time of 2.5 ms. Corresponding temperature, acetylene and soot mass fraction are presented in the second row of Figure 7. The number density field is seen to be similar to the soot mass fraction field. The peak levels appear to occur in a similar location both along the flame and in the mixture fraction bands at a given flame location. Number density appears to be more evenly distributed along the flame, however, as particles are generated solely by acetylene for the given soot model. As soot is transported away from reaction zones, particle coagulation occurs, reducing the number density and increasing particle size. Soot mass fraction levels are only affected by number density through the implicit mean particle size, which affects the surface area used in the rate calculation. Unlike number density, which is derived from the gas phase alone, soot mass fraction has the additional source arising from surface growth, which depends on the level of soot in the reaction zone. Thus, depending on soot transport into or out of reaction zones, local soot mass fraction levels can be concentrated or diminished.

This effect is evident by comparing the number density and nucleation rate fields, and the soot mass fraction and growth rate fields. The nucleation occurs all along the flame resulting in a more homogeneous number density field, whereas the soot growth rate field is concentrated along regions of negative flame curvature, just as

the soot mass fraction is. It is interesting to note that the soot oxidation rate also shows a high degree of variation along the flame, with peaks in the same locations as the growth rate, indicating that high levels of soot growth occur with high levels of soot oxidation. However, the location of the rates in the mixture fraction coordinate are different, as expected, with oxidation occurring at leaner mixture fractions than growth, though both are on the rich side of the flame where soot is present. The peak soot oxidation zones occur where the soot levels are at leaner mixture fractions. In these regions, the soot concentration is higher, and the oxygen concentration at the location of soot is higher. Both of these effects enhance the soot oxidation rate. Contours of oxygen concentration are not shown in the figure since they are negligible at the stoichiometric surface. OH mass fraction contours are shown to indicate the flame surface and reaction zone, and since OH is known to contribute to soot oxidation.

In Figure 8, there appears (visually) to be a strong correlation between the soot levels and rates and the flame curvature as well as scalar dissipation rate. These relations are discussed further below by considering global statistics and quantities along the flame.

#### 4.2. Global Statistics

Figure 9 shows scatter plots of soot mass fraction at times of 1.75 and 5 ms, and temperature, acetylene, soot growth rate, and nucleation rate at times of 1.75 ms, all versus mixture fraction. The mean stoichiometric scalar dissipation rates at the two times are  $14.2$  and  $5.5 \text{ s}^{-1}$ , respectively (the steady extinction value is  $148 \text{ s}^{-1}$ ). The low degree of scatter in temperature indicates that this flame is not highly strained and combustion reactions are mixing limited. The soot mass fraction plots reveal two important effects. First, the relatively slow soot growth and nucleation rates result in widely varying soot mass fractions at any given mixture fraction so that the scatter plot appears dense below its upper range. The soot mass fraction figure on the left at 1.75 ms has a scale five times less than the same plot on the right at 5 ms. At 1.75 ms the profile is rather smooth, with a peak at approximately  $\xi = 0.15$ , which corresponds to the locations of the maximum growth and nucleation rates. At 1500 K, a soot mass fraction of 0.02, 0.01 and 0.002 corresponds to volume fractions of 2.6, 1.3 and 0.26 ppmv, respectively, with the conversion given by  $f_v = \frac{\rho Y_s}{\rho_s} = \frac{191030 Y_s}{T} \text{ ppmv}$  assuming a soot density of  $1850 \text{ kg/m}^3$  and a gas molecular weight of  $29 \text{ kg/kmol}$  at 1 atm pressure.

Second, the soot mass fraction is transported in the mixture fraction coordinate. In time, the soot clearly migrates toward richer mixtures. The peak soot level is still at approximately  $\xi = 0.15$ , but substantial levels of soot are present at mixture fractions as high as 0.8. The scatter profile is also seen not to be smooth, but evidence of the transport of soot to large values of mixture fraction along coherent structures is observed as eddies convect soot away

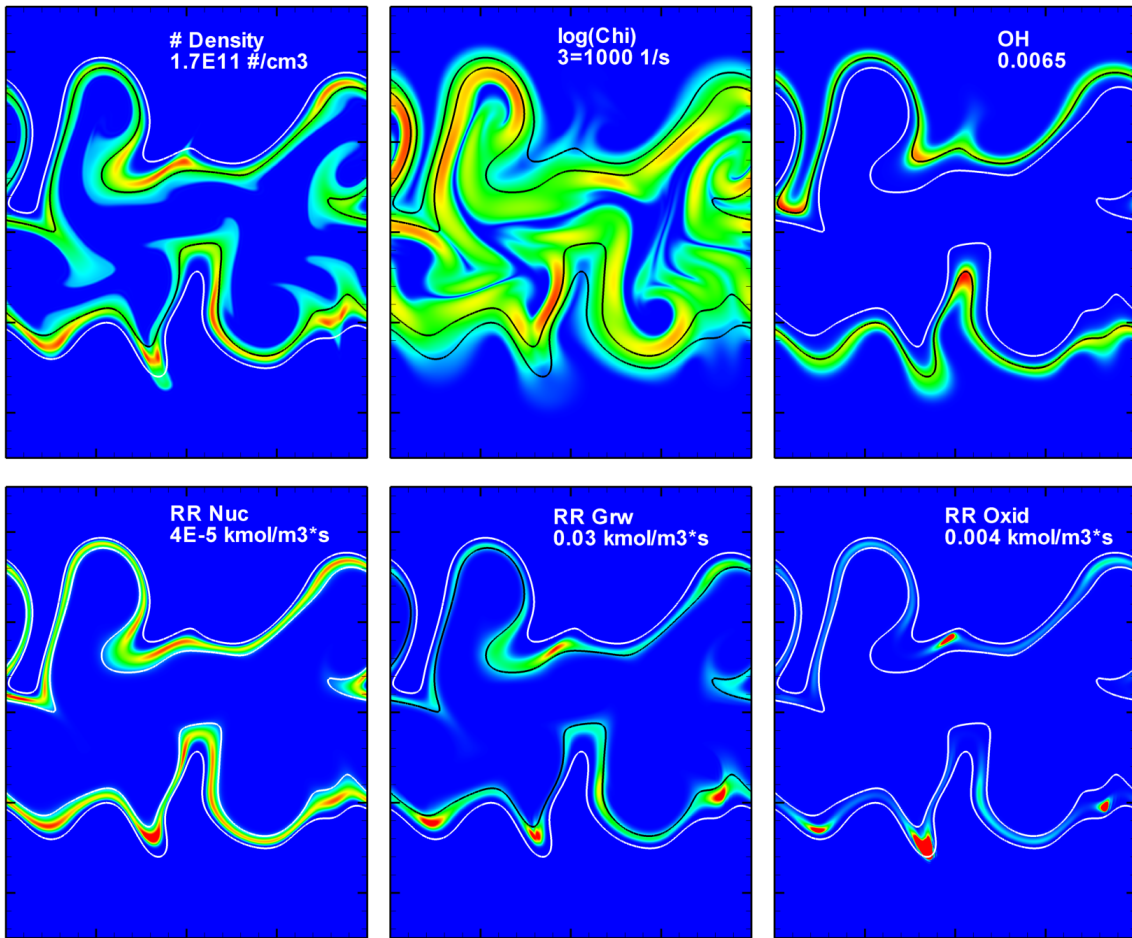


Figure 8: Scalar fields with indicated peak scale (red) at 2.5 ms with mixture fraction isocontours of 0.064, 0.2 (line color for clarity only). The peak soot nucleation, growth, and oxidation rate peaks are off scale at  $5.1E-5$ ,  $0.036$  and  $0.143$  kmol/m<sup>3</sup>s, respectively.

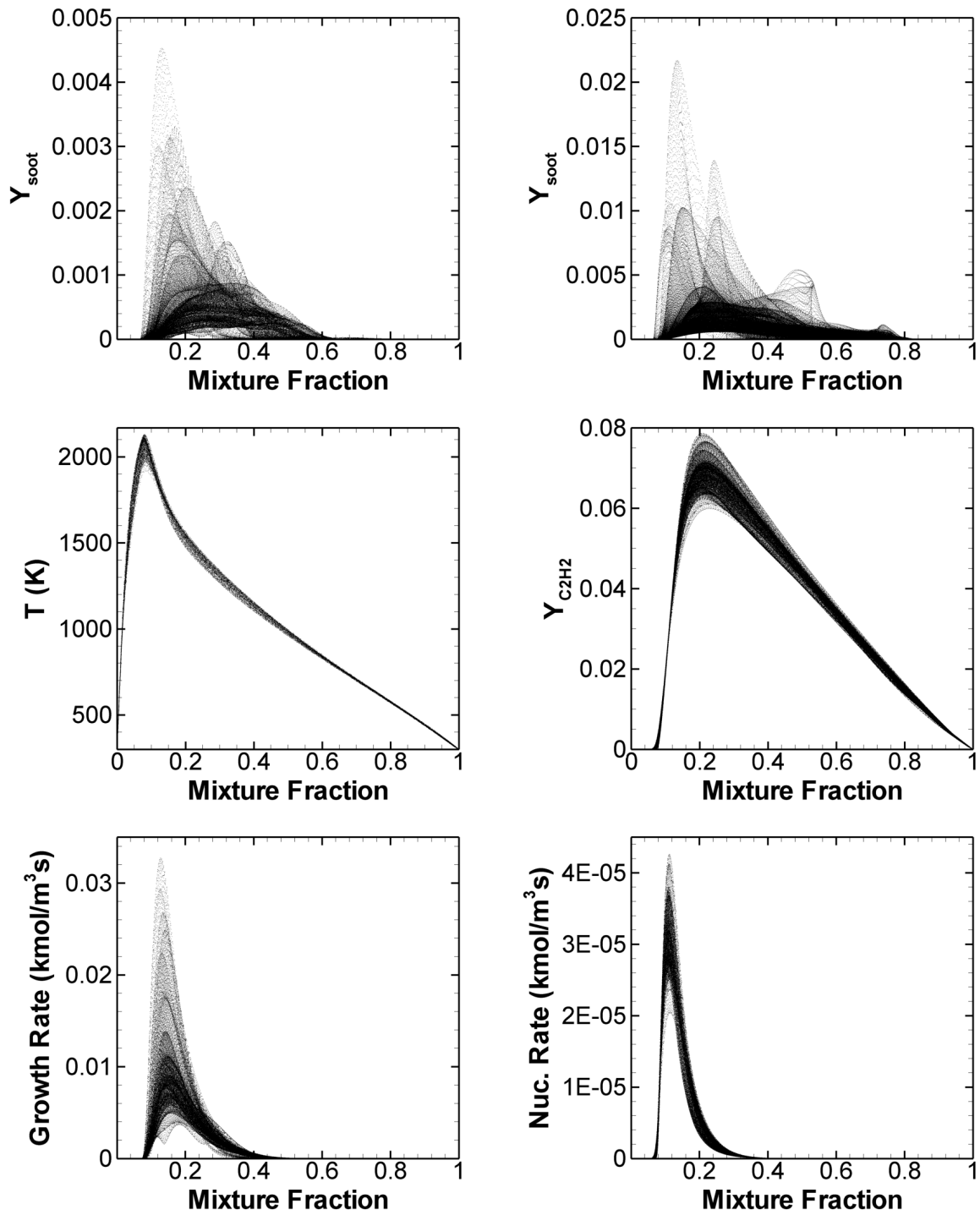


Figure 9: Scatter plots at 1.75 ms with soot mass fraction at 1.75 (left) and 5 ms (right). The temperature plot shows one in three indices in x and y.

from flame zones into the fuel core where mixture fraction diffusion increases the richness of the soot-gas mixture. The temperature, acetylene and rate profiles are shown at only one time since they are essentially the same at 5 ms, with the exception that the acetylene mass fraction and soot growth rate peaks are nearly twice as high, while the nucleation rate peaks at about  $5 \times 10^{-5}$  kmol/m<sup>3</sup>s. Unlike soot mass fraction, the soot growth and nucleation rate profiles are localized in the mixture fraction coordinate. This localization of the soot rates is well known and is due to the strong temperature dependence and locality of the gaseous species with respect to mixture fraction.

#### 4.3. Flame Displacement Velocity

Figures 7 and 8 clearly demonstrate the correlation between soot concentrations/rates and flame shape. The correlation is better understood by examining the displacement velocity of the flame relative to the fluid motion given by Eq. 13. Figure 10, plot (a) shows the stoichiometric flame displacement velocity relative to the fluid convective velocity as the two colored lines at 1.75 ms. Soot mass fraction is shown in grayscale, with a peak value colored at 0.002 (dark). The peak soot mass fraction is 0.0045 (or 0.46 ppmv) and occurs along the lower flame at the far right of the figure. Along the stoichiometric surface, fluid velocity vectors are shown. As discussed earlier, positive values of the flame displacement velocity correspond to the flame moving towards the fuel stream, while negative values denote flame motion towards the air stream. The convective velocity through the flame is opposite the flame displacement velocity, and for red zones soot will be convected into the flame. This figure shows that high soot levels occur with flame motion towards the soot. Clearly the highest levels of soot occur toward the red, positive regions of flame displacement velocity. History effects of transported soot are also evident in the figure, though minimized by the early time chosen here.

This figure generally confirms the behavior that was described and predicted in the Flame Analysis section. In relatively flat regions of the flame, the flame displacement velocity is negative (towards air) since this is the direction (sign) of the normal diffusion term of the flame displacement velocity shown in Eq. (15). Flame regions that are positively curved result in even higher negative flame velocities, while flame regions that are negatively curved are those with more positive flame displacement velocity. Figure 10 shows that fluid vectors are not strictly tied to the direction of the flame displacement velocity. We observe, for example, that there are regions of opposite flame displacement velocity with the fluid normal component pointing toward the air stream. This emphasizes the importance of the flame motion relative to the local fluid velocity.

Plot (b) of Fig. 10 is the same as plot (a) but with the stoichiometric surface colored by the scalar dissipation rate. As expected, the peak soot levels tend to occur in regions of low  $\chi$ . However, low levels of soot also occur in

regions of low  $\chi$ , especially where the flame surface is positively curved, such as along the lower flame near the center, and along the upper flame at the left. We note that in Plot (a), for  $v_\xi$ , in the same regions, there appear to be high concentrations of soot with negative values of  $v_\xi$ , contrary to the main correlation of soot and  $v_\xi$ . The analysis is somewhat complicated by the history effects of the soot evolution and the flame dynamics, which can change the magnitude of  $\chi$ , and the sign of  $\kappa$ . For example, the upper flame at the right shows a soot peak in a downward arch. The flame curvature at this position changes sign as the flow evolves, with the initial curvature centered in the fuel stream. This also occurs at the soot peak on the lower flame at the left, which can be seen in the time progression in Figure 7. As the flame displacement velocity accounts for the effects of both flame curvature and scalar dissipation rate (as discussed previously and shown in Eq. 16), it seems to be a better indicator of high soot regions.

At the 1.75 ms time shown in Fig. 10, there appears to be relatively little flame-flame interaction, with the flame structure varying from pure fuel to pure air across a given location of the flame. This allows analyzing the flame in the context of more traditional one-dimensional and flamelet models, to examine the importance of multidimensional effects.

#### 4.4. Flame Normals

The soot-flame interaction is examined in more detail by considering scalar profiles of temperature, composition, and reaction rates along flame normals. Representative individual results are presented at two spatial locations of opposite flame displacement velocity at 1.75 ms. Statistics considering all flame normals are presented later. The positions of the two normals considered are labelled in Fig. 10. Positions 1 and 2 have flame displacement velocities of 90 and -100 cm/s, respectively. The stoichiometric scalar dissipation rate values are approximately 3.5 1/s, and were chosen to be close in magnitude. The peak temperatures for these two cases differ by only 25 K. Plots of soot mass fraction, number density, acetylene mass fraction and soot rates of nucleation, growth and oxidation are shown versus mixture fraction in Figure 11.

The soot mass fraction profile is particularly interesting. At position 1, the flame displacement velocity is positive, resulting in the flame moving toward the convected soot particles. The opposite occurs at position 2, where the flame displacement velocity is negative. The soot peak of position 1 has a value of 0.003, at a mixture fraction of 0.121 ( $\phi = 2.0$ ). At position 2, the soot mass fraction peak is 0.0006, at a mixture fraction of 0.254 ( $\phi = 5.0$ ). The soot level at position 1 is a factor of 5 higher than at position 2, and peaks much leaner as well. The temperatures at the soot peaks for positions 1 and 2 are 1898 and 1358 K, respectively, a difference of 540 K. This difference in temperature, as well as soot level, strongly affects the soot contribution to the radiative source term. Figure 12 shows

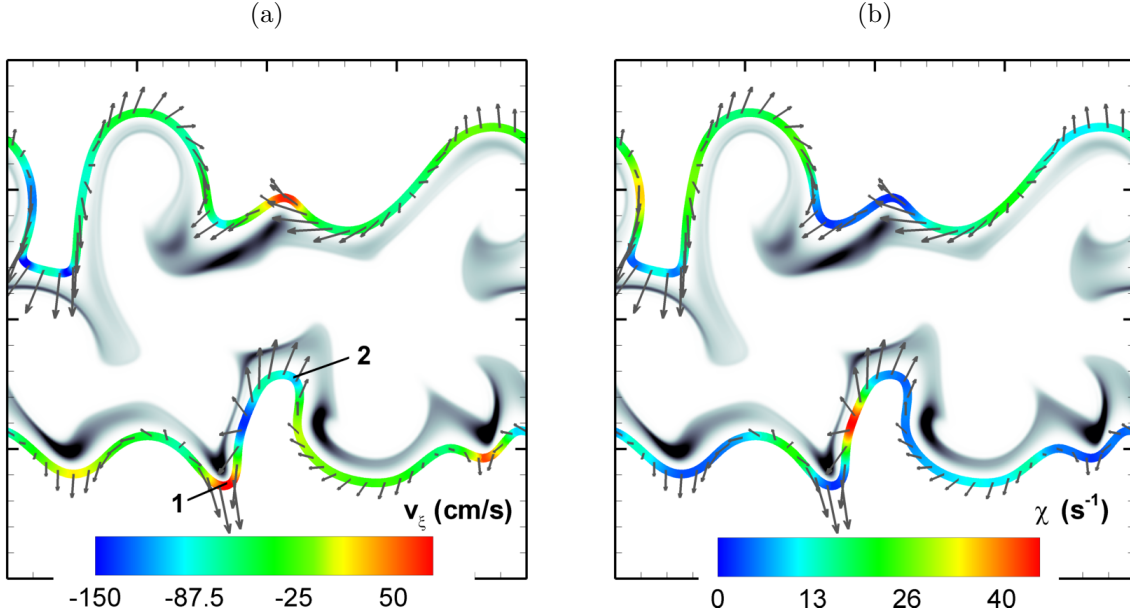


Figure 10: Soot field at 1.75 ms with stoichiometric surface colored by flame displacement velocity (a), and scalar dissipation rate (b). Vectors are fluid velocity. The soot mass fraction is shown in grayscale where the maximum value shown (dark) is 0.002.

the optically thin gas and soot radiative source terms at the two positions. These terms are given by

$$Q_{rad} = 4\sigma K(T^4 - T_\infty^4), \quad (17)$$

where  $\sigma$  is the Steffan-Boltzmann constant, and  $K$  is the gas or soot absorption coefficient. The ratio of the soot contribution to the optically thin radiative heat flux of position 1 to position 2 is 15 using values at the soot peaks. The gas radiation sources are similar while the soot radiation is substantially higher at position 1, even exceeding the gas source term. The total peak radiative transfer rate at position 1 is more than twice the total peak rate at position 2.

The width of the soot peak at position 2 is also much wider than at position 1. As the flame moves away from the soot, the soot peak is drawn out in mixture fraction, resulting in the profile spanning  $\xi = 0.1 - 0.6$ . Presumably, the soot peak at position 1 is also stretched as the flame moves into the soot, but the soot is oxidized as it approaches the flame, hence the profile is limited. This motion in the mixture fraction coordinate can only be explained by differential diffusion of the soot relative to the gaseous species comprising the flame. A close look at the soot mass fraction and number density profiles at position 2 shows a bimodal profile, consistent with production at lower mixture fractions coupled with transport toward higher mixture fractions. The number density profile is qualitatively similar to the soot mass fraction profile in its width and location. The difference in magnitude of the two positions is not as severe for the number density as for the soot mass fraction. This difference is similar to the difference in the nucleation rate peaks, the values of which are dependent upon differences in the acetylene concentra-

tion and temperature profiles. The shift in number density toward lower mixture fraction at position 1 is contrasted with the similarity in the locations of the nucleation rate peaks, which depends only on the gaseous environment, and further indicates the motion of the flame towards the soot at position 1.

In contrast to the soot profiles at both locations, the locations and widths of the profiles of the soot precursor, acetylene, as well as the soot nucleation and growth rate profiles, are nearly constant. The soot oxidation rate is a factor of 100 higher at position 1 than at position 2 as the soot is convected toward the flame zone into regions of higher oxidizer concentration.

Figure 11 shows profiles through two flame positions at a single point in time and emphasizes the fact that the flame motion can result in peak soot levels very close to the flame. Figure 7 shows the position of the soot peak relative to the mixture fraction contours at four times. At position 1 in Fig. 11, values at the peak level of soot are shown at times from 1 to 2.5 ms in Fig. 13. At later times the soot is oxidized by the flame, and as the flame folds together, two vertical soot zones appear, making further comparison difficult. As time progresses, the mixture fraction of peak soot decreases from 0.18 to 0.09, the temperature at peak soot increases from 1592 to 2139 K, and the soot volume fraction increases from 0.1 to 0.44 ppmv (assuming a mean molecular weight of the gas of 29 kg/kmol). The corresponding mass fraction varies from 0.00087 to 0.0049. These results clearly show the unsteady motion of the stoichiometric surface towards the soot peak as time progresses.

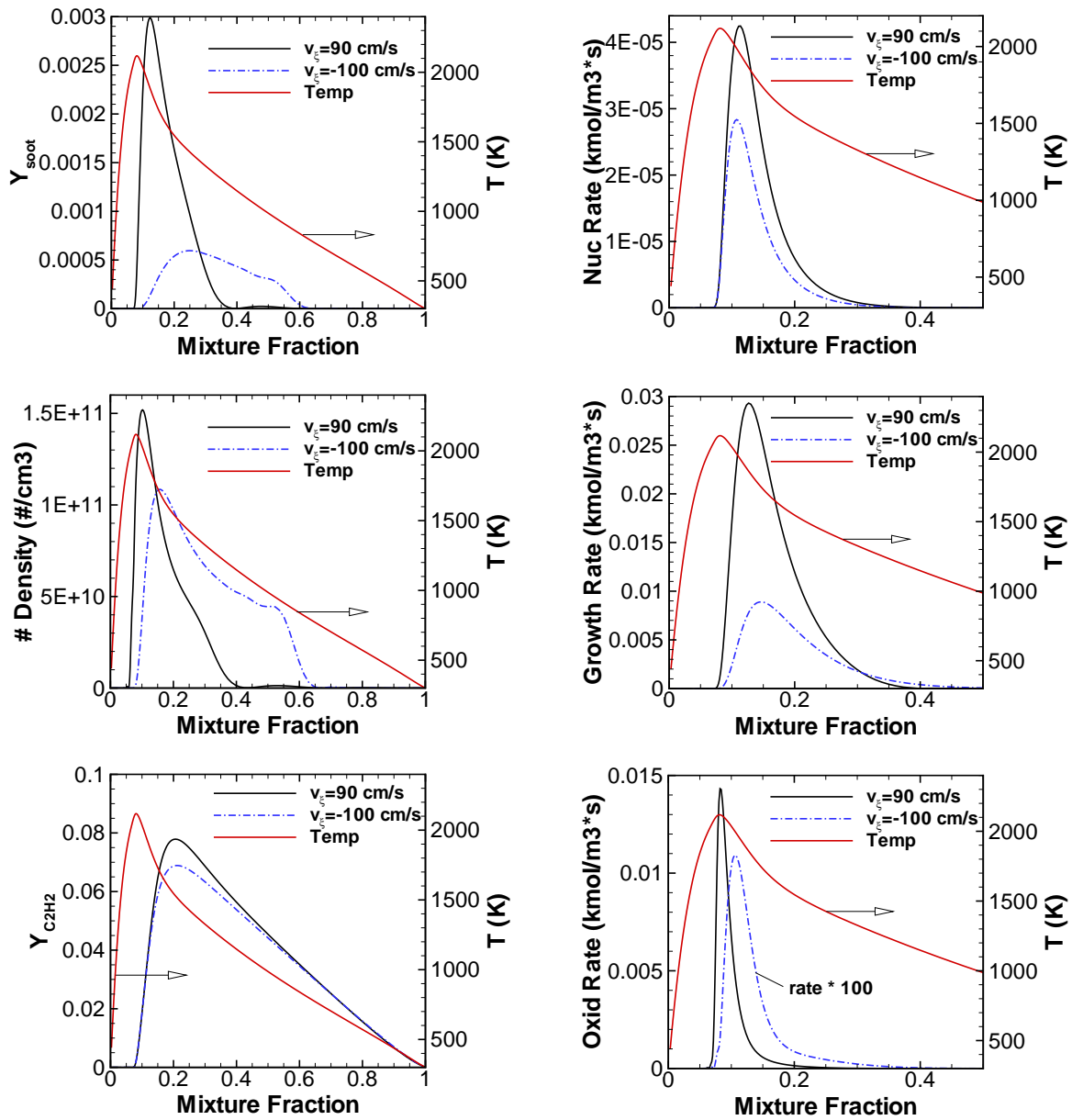


Figure 11: Plots along two flame normals shown in Fig. 10. at 1.75 ms.

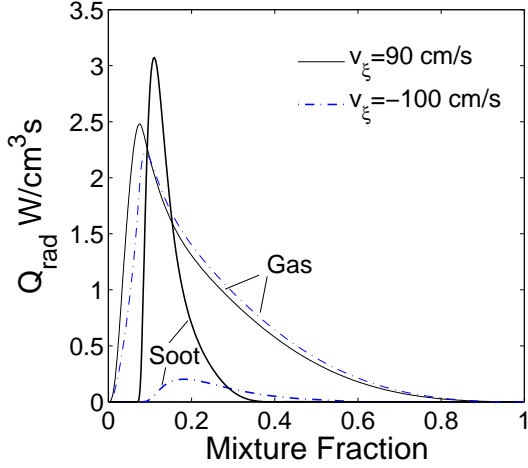


Figure 12: Gas and soot optically thin radiative source terms along flame normals at positions indicated in Fig. 10.

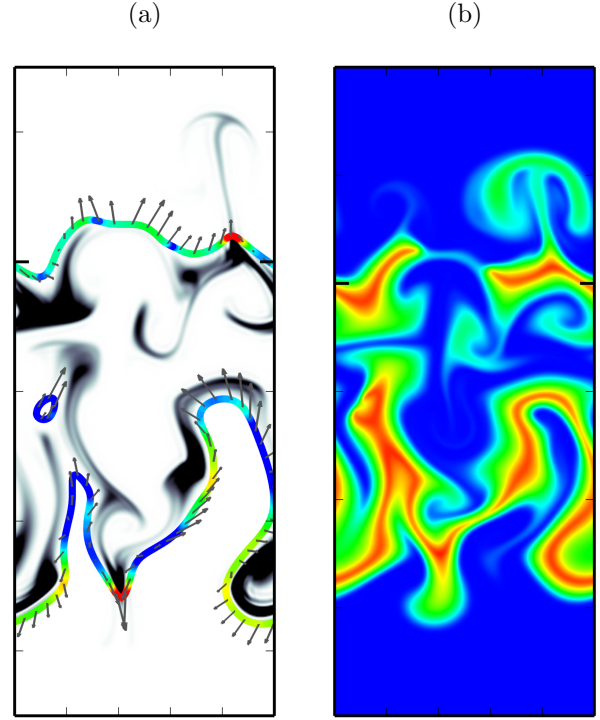


Figure 14: Alternate simulation results showing temperature (b) colored from 300 to 2200 K. Figure (a) corresponds to Fig. 10 showing stoichiometric surface colored by flame displacement velocity, with grayscale soot mass fraction field (black is 0.0002 or greater). The time is 1.14 ms. Note soot breakthrough at top left.

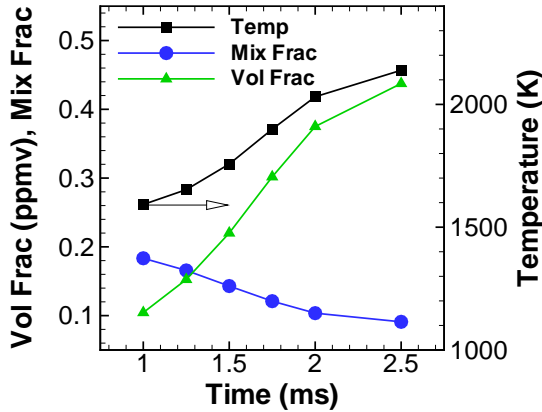


Figure 13: Soot concentration, temperature and mixture fraction at the peak soot level at times from 1 to 2.5 ms at the location corresponding to position 1 in Fig. 10.

#### 4.5. Soot-Flame Breakthrough

Soot-flame breakthrough is an important phenomenon and one that is not well understood. In fires, for example, large quantities of soot are commonly emitted, that can absorb radiation and shield the surroundings from radiative heat transfer. While the flow timescales of direct numerical simulation are small compared to fires, DNS allows detailed examination of soot-flame interactions. In the present simulation, soot was not observed to penetrate the burning flame zone. However, in another simulation, similar to the base case, but with a more vigorous turbulence field imposed, soot was found to break through the flame. Figure 14 shows the soot and temperature profiles of this alternate case at 1.14 ms. This case had a mean fluctuating velocity  $u' = 300$  cm/s, a turbulent integral scale of  $L_{11} = 0.133$  cm, and half the domain width at  $1 \times 3$  cm. The parameters of the baseline case are in Table 1. In the upper right side of image (a) the soot clearly breaks through the flame. Plot (b) shows the temperature field, clearly indicating that the flame is burning. There are regions in this flow for which the flame is quenched, as evident along the upper flame in the center. The soot mass fraction at the top of the stream is  $8.8 \times 10^{-5}$ , with a corresponding volume fraction of 0.015 ppmv. The peak soot mass fraction in the domain is 0.002 (0.2 ppmv) and occurs in the *ball* of soot at the lower right of the figure.

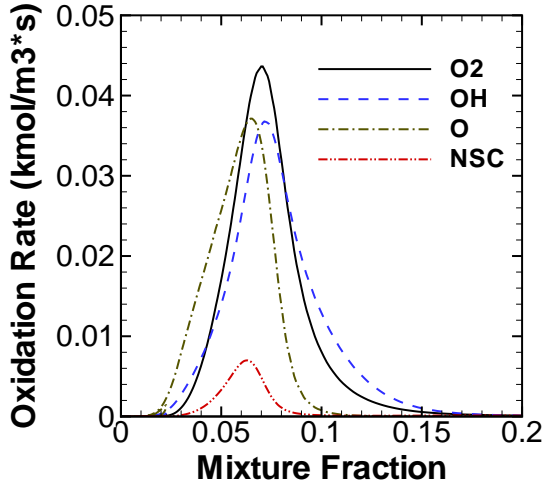
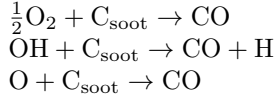


Figure 15: Plots of soot oxidation rates versus mixture fraction along a streamline through the flame at the point of soot breakthrough in Fig. 14.

Soot also breaks through to the lean side of stoichiometric at the central red cusp along the lower flame, but to a lesser extent at the time shown.

Consideration of soot-flame breakthrough calls into question the validity of the soot oxidation model used. Figure 15 compares profiles of soot oxidation rate for three oxidation reactions presented in [41]:



Rates for the reactions as given in [41], taken from [4, 42, 43] are

$$r_{O_2} = 10000e^{-19640/T}T^{1/2}[O_2]A_s, \quad (18)$$

$$r_{OH} = 106\phi_{OH}T^{-1/2}X_{OH}A_s, \quad (19)$$

$$r_O = 55.4\phi_O T^{-1/2}X_O A_s, \quad (20)$$

where  $\phi_{OH}$  and  $\phi_O$  are 0.13 and 0.5,  $X$  is mole fraction, and units are kmol, m, s, K, giving rates in units of  $kmol/m^3s$ .  $A_s$  is the particle surface area per volume given by

$$A_s = \pi \left( \frac{6\rho Y_s}{\pi n \rho_s} \right)^{2/3} n. \quad (21)$$

Figure 15 also shows the original Nagle–Strickland–Constable  $O_2$  oxidation rate [44] by way of comparison, which is smaller than the other rates.

The profiles in Fig. 15 are along a streamline through the point of soot breakthrough at the upper right of Fig. 14 at 1.14 ms. In this case, the OH, and the Leung and Lindstedt (L&L)  $O_2$  oxidation rates are very similar in magnitude, shape and position. The O oxidation rate is similar in magnitude and width, but occurs at a somewhat lower mixture fraction, which is consistent with its mass fraction profile. The rate given for the L&L  $O_2$  oxidation was used

alone in the present DNS simulations. In [4] it was noted that the oxidation rate constant for  $O_2$  oxidation was adjusted to match the maximum surface oxidation rate for laminar, co-flowing methane–air flames. Thus, effects of O and OH oxidation would be partially built-in to the oxygen rate. If the L&L  $O_2$  rate is taken as the sum of  $O_2$ , O, and OH reactions, then we have a discrepancy of about a factor of two: either the L&L rate is too low, or the other rates (together) are too high. We do not attempt here to provide a comprehensive treatment of soot oxidation, which is the subject of ongoing research. Rather, the phenomena of soot-flame breakthrough observed in the DNS calculations highlights an interesting, and potentially important mechanism for soot emission from flames. The quantitative results of the soot breakthrough in the DNS are subject to uncertainties in the soot growth and oxidation model, as noted, and also the representation of the particle size distribution, which, while common, is limited in the present, two-moment (i.e. monodispersed) approach. This model will tend to underestimate soot surface area, and hence soot reactivity.

It is worth emphasizing that the soot breakthrough computed here is different than what would be expected in larger-scale flames and fires. In those situations, increased flow residence times result in higher soot concentrations, hence increased radiative heat losses and flame chemistry interactions. In the present simulations, while the soot is fully coupled to the gaseous composition and energy flow fields, the soot concentration and residence times are too small to have a substantial impact on the temperature and composition of the flames. A soot concentration of 1 ppmv, corresponds to about 5% of the local fuel carbon. We have shown here that soot breakthrough is possible in a configuration for which soot breakthrough is not favorable. In real situations, as soot passes through a flame, the flame temperature will decrease due to radiative losses, and be further weakened, possibly to the point of extinction (allowing substantial soot emission), as flame radicals are consumed by oxidation of soot. Furthermore, higher soot concentrations occur with larger particle sizes, so the soot-area-to-mass ratio will be lower, reducing soot reactivity per unit mass, and tending to increase the amount of soot breakthrough.

#### 4.6. Normal Statistics

Figure 11 showed scalar profiles along two selected normals at a time of 1.75 ms. To further clarify the flame-soot interaction and structure, flame normal profiles were computed along the stoichiometric mixture fraction surface. Along a flame normal, the point of intersection of the normal with the flame, and the point of peak soot mass fraction,  $Y_{\text{soot}}^*$ , are of particular interest. Figure 16 shows values of the mixture fraction and temperature at peak soot (denoted  $\xi^*$  and  $T^*$ , respectively) along the normal versus the stoichiometric flame displacement velocity  $v_\xi$ . These plots show a clear correlation between the location of the peak soot in the mixture fraction coordinate

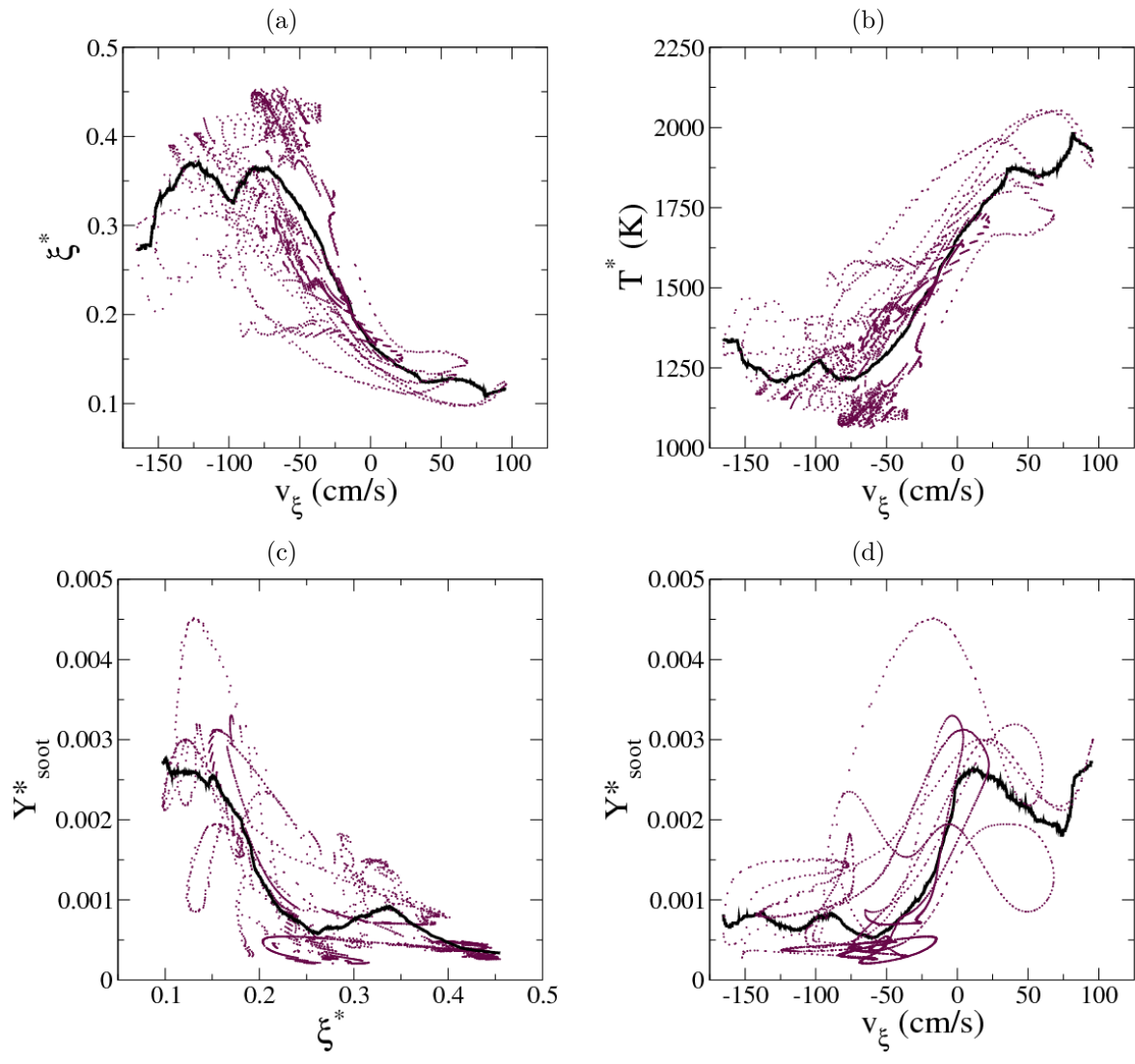


Figure 16: Scatter plots along flame normals at 1.75 ms. Starred symbols correspond to values at peak soot mass fraction along flame normals. Solid lines are moving average of data with a window size  $1/10^{th}$  the domain of the data.

and the flame displacement velocity. Where  $v_\xi$  is shifted towards positive values through negative flame curvature, the peak soot occurs at lower mixture fraction, closer to the flame, hence at a higher temperature where reaction and radiative rates are higher. Higher values of  $v_\xi$  tend to occur in regions of negative flame curvature. In these regions, the effect of thermophoresis is to focus the soot, increasing soot concentrations. However, we show below that thermophoretic effects are relatively small, and elevated soot concentrations are dominated by the proximity of the soot and flame.

While there are not a lot of data points at the highest levels of the flame velocity, the  $\xi^*$  data appear to be levelling off there. This is consistent with the soot reaching an oxidation barrier near the flame surface. The presence of soot breakthrough would show up in soot at mixture fractions below stoichiometric (0.064).

The plot of peak soot mass fraction versus  $\xi^*$  in the figure shows a strong correlation between the level of soot and the location of the soot in the mixture fraction coordinate, with a spread of a factor of 22 in soot mass fraction with peak levels ranging from mixture fractions of 0.1 to 0.45. Hence, at higher  $v_\xi$ , plots (a) and (b) show that the peak soot is closer to the flame, and at a higher temperature, while plot (c) shows that the soot concentration is higher when the peak mixture fraction is lower. In plot (d), the  $Y_{soot}^*$  is shown versus  $v_\xi$ , which is essentially a combination of plots (a) and (c). Here, the data shows more scatter, and the correlation of peak soot concentration along a flame normal with the flame displacement velocity is not as obvious, although the soot concentration is higher at higher flame velocity. Note, however, that plot (d) is also correlating two spatially segregated points along a flame normal, where the soot concentration grows in time. Regions of positive and negative  $v_\xi$  are conceptually similar to normal and inverse co-flow diffusion flames, respectively. Our results are consistent with experimental observations of lower soot concentrations in inverse diffusion flames than normal diffusion flames [7].

Although not shown here, the peak soot mass fraction is observed to be correlated as expected with the two terms of the flame displacement velocity equation, and not just their sum. That is,  $Y_{soot}^*$  is highest in regions of low scalar dissipation rate and more negative flame curvature. Low scalar dissipation rates, alone, imply higher flame temperatures and longer residence times for soot nucleation and growth reactions. Negative flame curvatures, in addition to shifting the relative flame motion towards the fuel (resulting in soot at lower mixture fractions with higher temperatures), will increase the temperature in the fuel-rich soot growth area through thermal focusing, further promoting soot growth. The low degree of scatter in the temperature-mixture fraction plot of Fig. 9 (about 100 K), compared with the strong dependence of temperature at peak soot in Fig. 16, shows that thermal focusing effects are secondary to curvature induced flame motion. Note that the relatively low degree of scatter in the tempera-

ture plot of Fig. 9 includes the relatively strong effects of the full range of scalar dissipation rates. A similar plot of temperature versus mixture fraction conditional on scalar dissipation rate would show a smaller temperature variation associated with effects such as thermal focusing.

Figure 16 also indicates the distribution of the flame displacement velocity with most of the data having negative values of velocity. Figure 17 plot (a) shows the PDF of  $v_\xi$  at 1.75 ms. The mean  $v_\xi$  is -45.7 cm/s and the standard deviation is 42.9 cm/s, and 13% of the velocity data are at positive velocity. The mean  $v_\xi$  is negative since the normal diffusion component is negative (see Eq. 15) while the mean of the flame curvature is nearly zero, as shown in plot (b) of the figure. The standard deviation of the flame curvature PDF is  $6.6 \text{ cm}^{-1}$ .

The flame displacement velocity  $v_\xi$  has been used to correlate the flame-soot interaction. This quantity is made up of curvature and normal diffusion terms as shown in Eq. (15). The relative importance of these terms is shown in Fig. 18 where a scatter plot of the curvature (first) term in Eq. (15), plot (a), is compared to the normal diffusion term, plot(b), versus  $v_\xi$ . The strong relation between the flame curvature term and  $v_\xi$  indicates the importance of this term, especially near the extrema of the range of  $v_\xi$ : the highest and lowest values of flame displacement velocity occur with low and high values of flame curvature. The normal diffusion term is restricted in magnitude to smaller values than the range of the curvature term for this flame, but in general we can see that both terms are of similar magnitude as has been previously observed [39]. The normal diffusion term is negative over nearly all of the flame, consistent with the stoichiometric mixture fraction being on the lean side of the inflection point in Fig. 6.

It is well known from one-dimensional studies that soot levels are reduced as strain rate increases due to lower formation times and reduced flame temperatures, e.g. [10]. The scalar dissipation rate is related to the flame displacement velocity through the normal diffusion term since higher mixture fraction gradients give rise to both higher normal diffusion and higher dissipation rate. The lower two images of Fig. 18 show the two terms of  $v_\xi$  versus the scalar dissipation rate. The mean curvature is defined above as the divergence of the mixture fraction iso-surface normal vector field, so as a normal with unity magnitude, we would not expect much relation to the scalar dissipation rate. Figure 18, however, shows that the magnitude of the curvature term is small at high scalar dissipation rates, consistent with the known fluid mechanical effect of mixture fraction iso-contours aligning with the strain field, which should reduce flame curvature in regions of high strain. The correlation of the normal diffusion term with the scalar dissipation rate is strong as expected, with higher dissipation rate resulting in more negative flame displacement velocity.

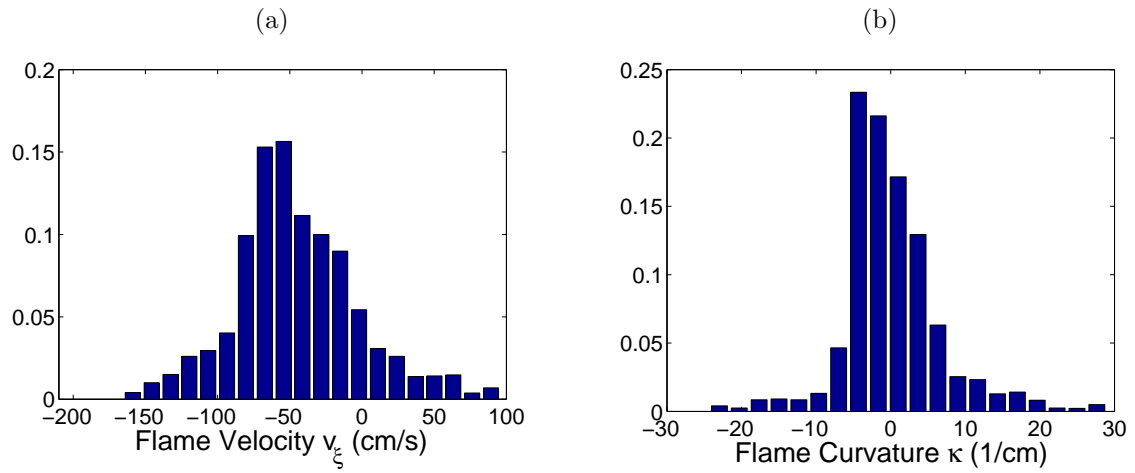


Figure 17: PDF of relative flame displacement velocity  $v_\xi$  and flame curvature at 1.75 ms.

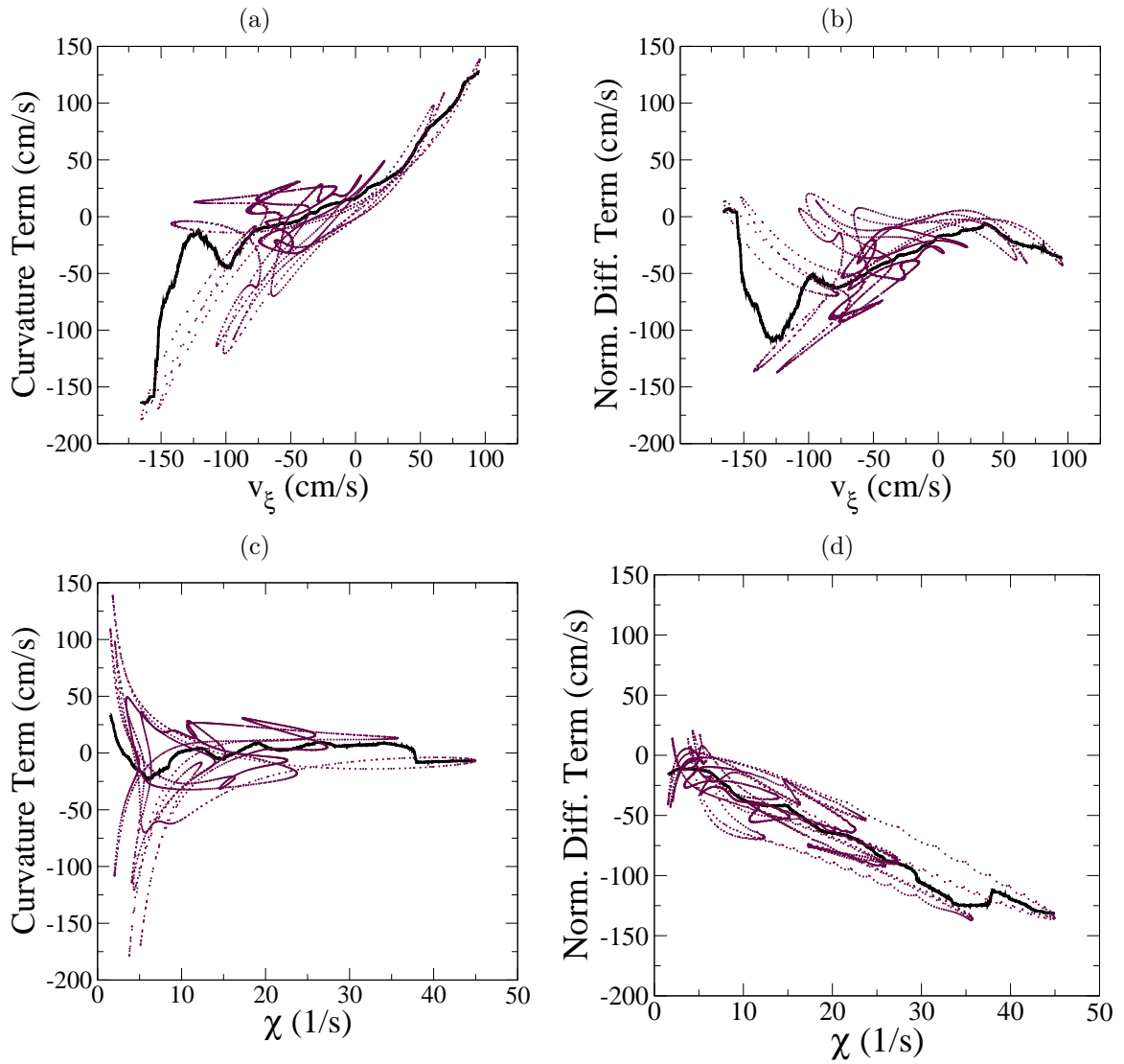


Figure 18: Scatter plots of curvature and normal diffusion term components of  $v_\xi$  versus  $v_\xi$  and  $\chi$  at 1.75 ms. Solid lines are moving average of data with a window size  $1/10^{th}$  the domain of the data.

#### 4.6.1. Temporal Evolution of Mean Flame Quantities

Figure 19 shows the flame surface area-weighted mean and standard deviation of flame quantities as a function of time. The flame displacement velocity, soot mass fraction and mixture fraction at peak soot along normals, and stoichiometric scalar dissipation rate are shown, as well as the relative flame surface area, and the fraction of flame area with positive flame displacement velocity. The maximum number of flame normals considered was 3789. The initial transient, as evident in the  $v_\xi$  and  $\chi$  profiles, is observed at times less than about 0.4 ms in which the strained flame relaxes and turbulence begins to wrinkle the flame.

An obvious anomaly is observed in the flame displacement velocity profile at a time just under 3 ms in which the flame displacement velocity spikes downwards. This is observed in part because of the limited size of the simulation providing a limited amount of flame area. This negative spike occurs as two flame sheets merge and quickly propagate under the influence of a strong positive curvature, leaving a faint trail of soot in its wake. In Fig. 7 this flame motion occurs at the flame cusp along the upper flame sheet at the far left of the domain and corresponds to the sharp drop in the relative flame surface area profile shown in Fig. 19.

The mean flame displacement velocity, shown in the upper left plot of Fig. 19, is negative at all times, but decays in magnitude as the turbulence field decays and scalar gradients relax diffusively. A mean velocity away from the fuel core (in mixture fraction) is expected initially, but for a finite fuel core surrounded by air, eventually the stoichiometric flame surface will move inward toward the center and disappear as the air stream diffuses into the fuel stream. So eventually, the mean flame displacement velocity has to become positive. The fraction (based on flame points) of flame displacement velocity greater than zero increases in time as does the flame displacement velocity, and varies from 0-15%, but is in the range of 10-15% for most of the simulation.

The mean stoichiometric scalar dissipation rate decays continuously from a value of 29 to  $5.5 \text{ s}^{-1}$ , with the initial transient rapidly reducing the dissipation rate to  $16 \text{ s}^{-1}$  at 0.4 ms. The mean of  $Y_{soot}^*$  along flame normals increases continuously from zero to 0.0033 ( $f_v \approx 0.35 \text{ ppmv}$ ). The mean of  $\xi^*$  along flame normals is initially quite lean at the location of peak production. As time passes, soot thermophoretically diffuses towards higher mixture fractions and the flame on average is moving away from the soot, resulting in the mean peak soot mixture fraction initially increasing with time. A peak is reached near the middle of the simulation after which the mean peak mixture fraction appears to level off and decrease slightly. So, soot is produced at low  $\xi$ , moves toward higher  $\xi$  under thermophoresis and negative flame displacement velocity, and levels off/decreases as the flame displacement velocity magnitude and flame gradients (e.g. temperature) are reduced while the soot formation region is relatively con-

stant (as shown below) at  $\xi \approx 0.15$ .

The standard deviation of the flame and flame normal data are given along with means in Fig. 19 and are seen to be of similar magnitude as the mean quantity, though plotted on a separate scale for clarity. The mean flame curvature is approximately zero throughout the simulation, but the mean curvature magnitude increases from zero to a maximum of  $4.9 \text{ cm}^{-1}$  at about 1 ms, and decays to values between 3.5 and 4 at times above 2.5 ms. The standard deviation of flame curvature rises to a fairly constant value of about  $6 \text{ cm}^{-1}$  at 1 ms.

The relative flame surface area varies over a range of about a factor of two in the simulation. Initially the flame area increases, reaches a maximum at 2.85 ms, and then decays as turbulence decays and flame curvature is reduced. This is about the same point as the mean peak in  $\xi^*$  in time.

#### 4.7. Temporal Evolution of Total Soot and Radiation

Of interest in the present discussion of the interaction between flame and soot is the overall amount of soot that resides in regions of negative curvature and positive flame displacement velocity. Weighted PDFs of curvature and mixture fraction isocontour displacement velocities were computed throughout the flow field (not just at the flame surface or along flame normals). The PDFs were weighted by  $\rho Y_s$ , soot growth rate, and the soot radiative source term. For example, the PDF of  $v_\xi$ , weighting with  $\rho Y_s$  is

$$P_{\rho Y_s}(v_\xi) = \frac{\langle \rho Y_s | v_\xi \rangle P(v_\xi)}{\langle \rho Y_s \rangle}. \quad (22)$$

This expression would be a Favre (density) average if  $\rho$  were used in place of  $\rho Y_s$ . Physically,  $P_{\rho Y_s}(v_\xi) dv_\xi$  is the fraction of soot mass in the domain that is in the range  $v_\xi$  to  $v_\xi + dv_\xi$ , where, in this section,  $v_\xi$  is at any mixture fraction, not just stoichiometric.

Figure 20 shows  $P_{\rho Y_s}$  at 1.75 ms in plot (a). The shaded region is one minus the cumulative PDF and represents the total fraction of soot that has positive  $v_\xi$ . This quantity is shown as a function of time in plot (b) for the cumulative PDFs of  $v_\xi$ , and also curvature  $\kappa$  (again, for any  $\xi$  surface), weighted by  $\rho Y_s$ , volumetric soot growth rate, and soot radiative source term. Here  $F$  denotes a cumulative weighted PDF. From plot (b), we see that up to 30% of the radiative source term occurs at positive  $v_\xi$ , while up to nearly 70% resides in regions of negative  $\kappa$ . We expect a significant portion of the radiative source term to reside in positive  $v_\xi$ , negative  $\kappa$  since the soot temperature is higher there and the radiative source is nonlinear with temperature. A significant fraction (up to 20%) of the total soot resides in regions of positive  $v_\xi$ . As noted previously,  $v_\xi$  is initially negative in the domain, as reflected by the lower set of curves. That we do not have higher fractions of radiation and soot mass in regions of positive  $v_\xi$  is a reflection of the relatively small portion of the domain with positive  $v_\xi$ . Note, however, that the critical

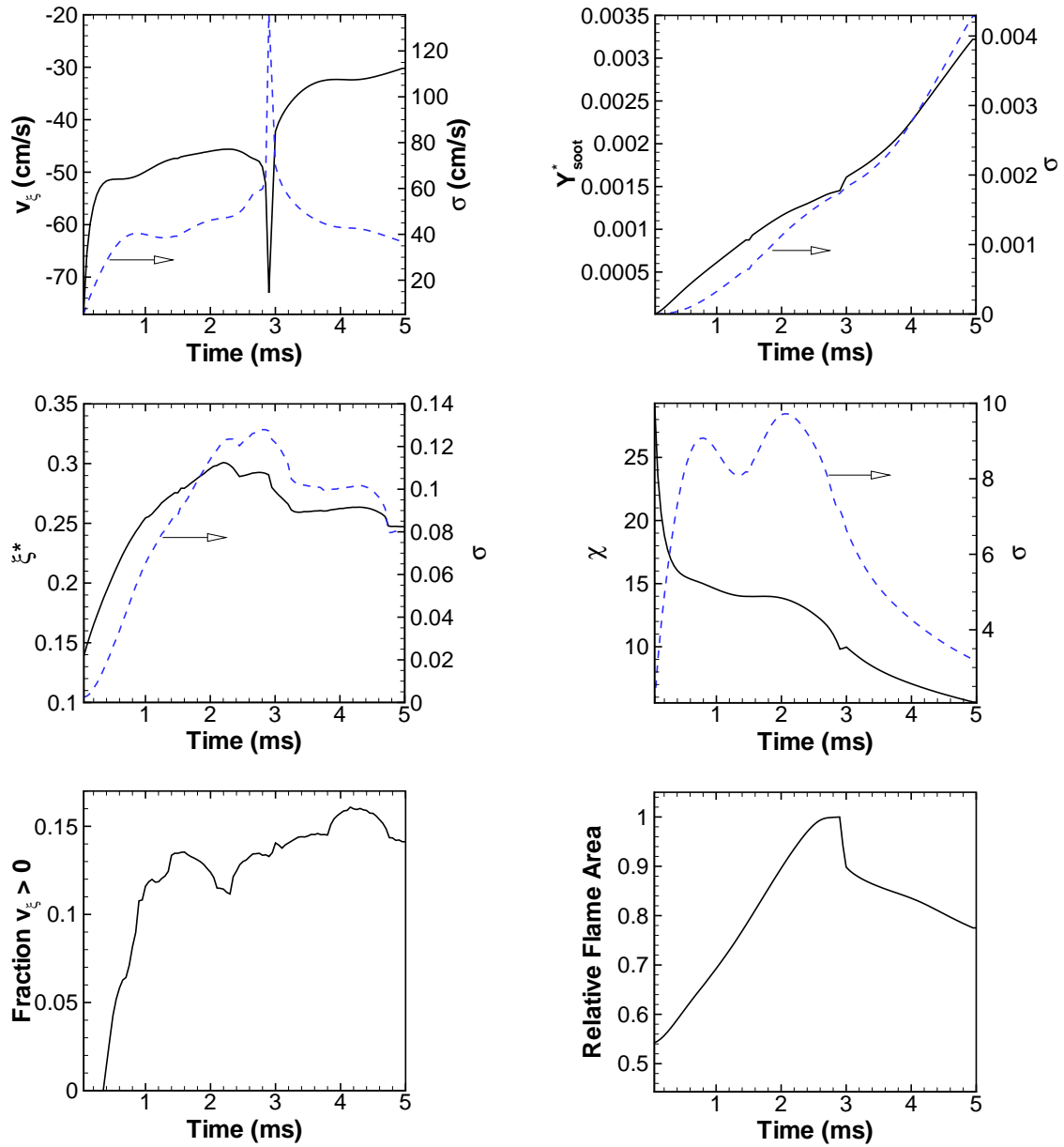


Figure 19: Time average quantities and standard deviations along the flame, or along flame normals in the case of soot mass fraction and mixture fraction at peak soot.

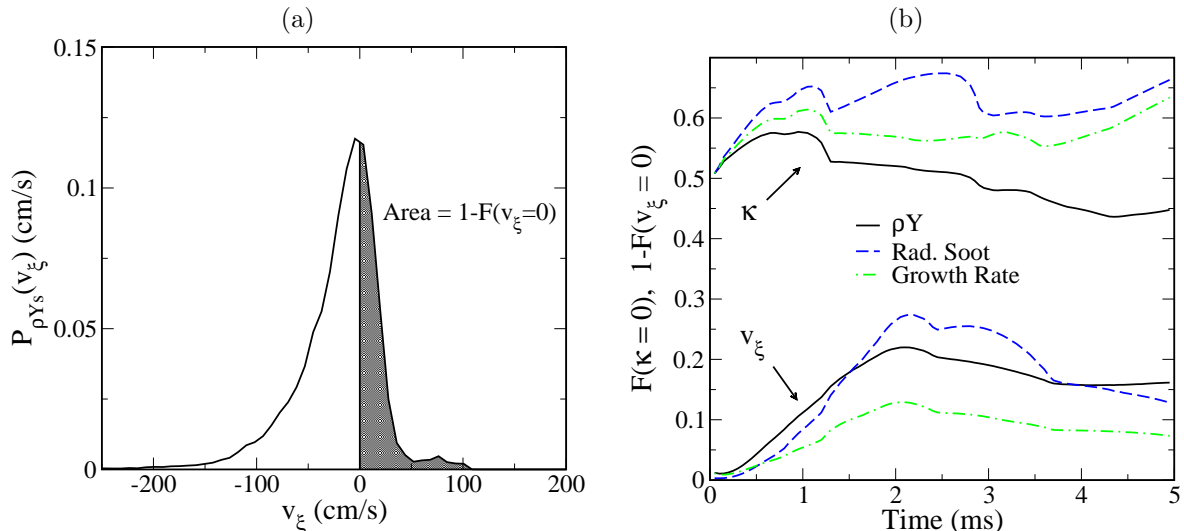


Figure 20: PDF of  $v_\xi$  weighted by  $\rho Y_s$ , (a), with one minus the cumulative PDF shown shaded, at 1.75 ms. Plot (b) is the temporal evolution of the cumulative weighted PDF. The upper curves are PDFs of  $\kappa$  and the lower are PDFs of  $v_\xi$ . Individual curves are PDFs weighted by the indicated quantities.

value of  $v_\xi = 0$  used here is somewhat arbitrary since  $v_\xi$  can be positive or negative depending on the competition between the curvature and normal diffusion components, and soot is shifted towards the flame for all positive curvature. Even though the fraction of soot mass and radiative source in positive  $v_\xi$  and negative  $\kappa$  are not overwhelming, they are still significant, and occur through multidimensional effects that are not captured in most standard models that neglect these effects.

#### 4.8. Soot transport

Soot transport is due to thermophoretic diffusion and fluid convection. The importance of these terms in relation to the flame motion is depicted in Fig. 21. The upper two plots show profiles through the two normals listed in Fig. 10, similar to Fig. 11. Each plot contains the flame displacement velocity, the normal component of the thermophoretic diffusion velocity,  $V_{thm}$ , and normal,  $V_{c,n}$ , and in-plane,  $V_{c,t}$ , components of the convective velocity. The in-plane convection is always positive since there is no directionality associated with it. The normal velocities are components in the direction of the local mixture fraction gradient. Note that the thermophoretic velocity is multiplied by a factor of ten, which, on the current plots shows that its value is about an order of magnitude below both the fluid convection and flame velocities. For this reason, we have considered the soot to be largely convected with the fluid. The thermophoretic velocity is similar at both positions and has values ranging from -10 to 10 cm/s over the whole mixture fraction range (the velocity is defined even where there is no soot), but has values of 6.8 and 4.5 cm/s at  $\xi = 0.2$  at positions 1 and 2, respectively. These values are in agreement with those found by Kang et al. [15]. The in-plane component of the thermophoretic diffu-

sion velocity is less than 5% of the normal component and is ignored here.

Note that the normal, and in-plane components of flow velocity are of similar magnitude at these two positions. This is important because (ignoring the flame displacement velocity), soot is convected as much toward or away from a flame as along a flame. If the curvature scales are of similar magnitude relative to the mixture fraction gradients, multidimensional effects will affect the soot history as the soot passes through the flow field. We also observe that in this flame, the flame displacement velocity is of a similar magnitude as the convective velocities, with values ranging from 0 to 100 and 0 to -200 cm/s at positions 1 and 2, respectively.

The lower two images of Fig. 21 show scatter plots of the flame displacement velocity and thermophoretic velocity versus the mixture fraction. Here again the flame displacement velocity tends to dominate the thermophoretic velocity for the interesting mixture fraction range from 0.1 to 0.4, above which the two velocities are comparable.

## 5. Discussion

The previous results have concentrated on the location of soot in the mixture fraction coordinate and the dependence of this locality on the dynamics of the soot-flame interaction. As noted previously, the location of soot determines its temperature and quantity, both of which impact soot yield and radiative heat transfer. A practical importance of understanding soot-flame interactions, which DNS alone can provide, arises through the need for turbulence-chemistry closures for RANS and LES models. Soot modelling in these contexts has been a challenge because of its complex chemistry, particle size distribution, optically thick radiative heat transfer, and long reaction

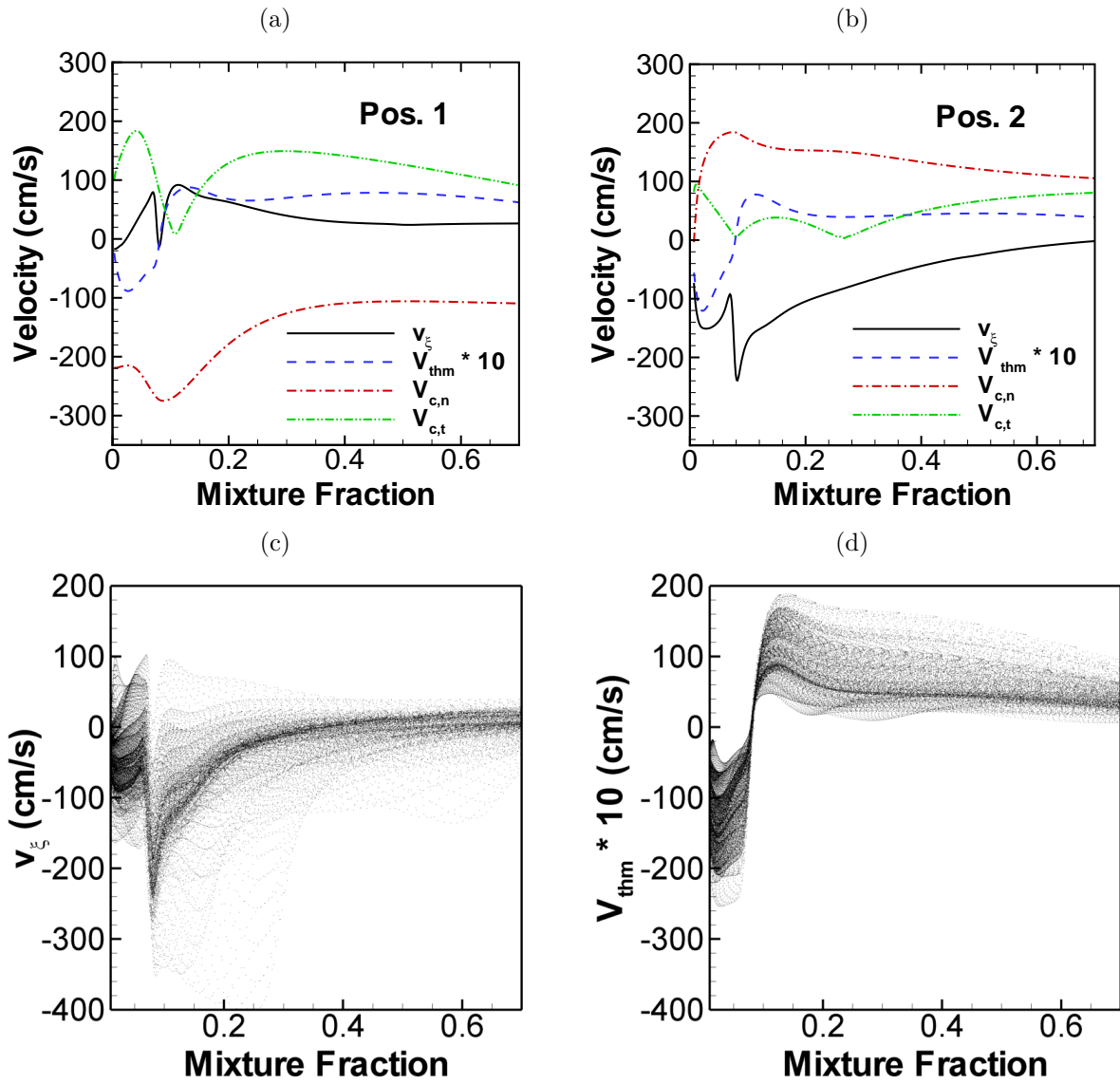


Figure 21: Profiles of flame displacement velocity, the normal component of thermophoretic diffusion velocity, and normal and in-plane components of convective velocity through two flame normals at positions in Fig. 10, (a) and (b). Figures (c) and (d) show scatter plots of normal thermophoretic diffusion and flame displacement velocity versus mixture fraction (skipping every other point in x and y for clarity). Simulation time is 1.75 ms.

timescales implying long history effects that must somehow be tracked through a flame.

Transporting detailed chemistry in CFD is usually too expensive and subgrid reaction models are often used to simplify the chemical description. Fox provides a good review of models for turbulent reacting flow [45]. A common approach that is illustrative of important modelling issues, and which has been widely applied to modelling sooting turbulent flames is the steady laminar flamelet model and its variations [46]. Here, mixture fraction and scalar dissipation rate are computed at the grid level, while all detailed chemical effects are computed separately by generating a library of one-dimensional flame solutions parameterized by mixture fraction and stoichiometric scalar dissipation rate. Mean quantities are obtained by convolving scalar variables over the joint PDF of mixture fraction and dissipation rate.

Soot modelling has provided a challenge since, as shown in Fig. 9, soot does not have a clean one-to-one state relationship with mixture fraction that is often observed in other quantities such as temperature. This has been shown here to be due to both the unsteady reaction of soot and the differential transport; these effects must be properly accounted for in order to obtain an accurate representation of soot. Differential diffusion is usually handled by assigning a large Lewis number to the soot species, or by accounting for the thermophoretic diffusion, which, for flamelets solved in mixture fraction space, requires a treatment such as that given in [47]. The unsteady effects have been accounted for by transporting one or more soot moments at the grid level, and computing the soot rates normalized by the soot quantity in the subgrid model [48]. Pitsch et al. used an unsteady flamelet model to capture the soot timescale and correlated the flamelet time to the spatial location in a turbulent jet flame to account for the unsteady soot growth [27].

Flamelet models as well as stochastic models such as the Linear Eddy Model rely on a one-dimensional description of the flame zone. In this paper, we have shown that multidimensional effects can significantly impact the interaction between the soot and the flame, through flame shape and displacement velocity. Consequently, one dimensional descriptions are not adequate for flames with significant multidimensional effects. To properly account for variable flame velocity effects in one-dimensional models, a correction would have to be applied for the differential soot transport. To this end Van Kalmthout and Veynante have modelled the mean flame displacement velocity in nonsooting turbulent nonpremixed flames in terms of the mean flame curvature and the normal diffusion component written in terms of the solution of an unsteady unstrained flame solution [39].

We have shown that soot breakthrough in a flame is possible, though only small concentrations are observed in the DNS simulation due to the relatively short simulation time. Soot-flame breakthrough is an important problem in large-scale fires where large amounts of soot can be

present on the outside (air side) of a flame, resulting in shielding of radiative heat transfer to the surroundings. Modelling this process is important if simulations are to yield correct heat transfer rates. However, the fundamental mechanisms for how soot can be formed in fuel rich regions and end up on the outside of a fire without first being oxidized are not fully understood. Although the time and length scales of DNS cannot approach those of fires, DNS is currently the only tool available for detailed examination of soot-flame interactions, and may lend insight into soot breakthrough and other phenomena. For example, we have observed the motion of soot towards higher and higher mixture fractions as time progresses. In flames with long timescales, downstream flames will likely exist between air and soot-loaded fuel that may increase the possibility of soot breaking through a burning flame, and may result in flame quenching through a combination of strain and radiative heat loss, allowing soot to escape to colder fuel-lean regions.

The semi-empirical soot mechanism employed in this work was chosen as a reasonable compromise between complexity, computational cost, and existing uncertainty in soot modeling, as discussed above. The mechanism does not include detailed soot chemistry involving combustion intermediates such as OH and H radicals. Soot growth and reaction steps are written in terms of acetylene, whereas soot nucleation is known to occur where PAH concentrations are high. Physical phenomena such as these will affect the location of the soot reactivity, and may be expected to alter the soot concentrations and locations within the flame zone. However, the primary result of the paper is that differential diffusion between soot and the mixture fraction directly shifts the soot into or out of the *bulk* flame zone. The soot reactivity depends not only on gaseous species concentrations, which are largely tied to the reactive flame zone, but also on the soot concentration in those reaction zones. We have shown that differential diffusion of soot results in soot transport over nearly the full span of mixture fraction. Hence, we believe that while the details of the soot mechanism will have an impact on soot concentrations, we would still expect to see higher soot concentrations in regions of more positive  $v_\xi$ .

Computational costs have dictated the DNS run time of 5 ms used. However, we expect the soot-flame interaction results of this work to be similar under turbulent conditions at longer times. We have noted that soot growth timescales are longer than those typical of combustion reactions, but that local (to single flame sheets) turbulent soot-flame interactions occur over shorter timescales than those based on global flow quantities (like timescales derived from jet exit velocities and location of peak mean soot concentrations). At longer times, we would expect higher levels of soot due to slower mixing rates of the decaying turbulence, as well as history effects as soot grows almost indefinitely given a hot, rich environment. However, the important velocities discussed (convection, thermophoretic, and flame displacement) depend on the soot

concentration only indirectly through the temperature, density, and gas composition fields, so we may expect similar behavior under similar turbulent conditions at higher soot levels.

The simulations presented in this paper are 2D dimensional, and we have focused attention on soot-flame interactions in flames wrinkled by turbulence, rather than on turbulent statistics, which are not available in the present simulation. However, as the primary interest is in real turbulent flames, from which we hope DNS can lend insight, the degree to which we would expect the results of this paper to carry over to three dimensional turbulence are important. The flame displacement velocity has been used to quantify the soot-flame interaction. This velocity arises from flame curvature and normal diffusion (i.e. flame strain). Qualitatively, 3D turbulence will curve and strain a flame sheet as we have seen in the present simulation. Quantitatively, the relative importance of the curvature and strain terms in Eq. 15 may vary. However, we have shown in the present simulation that both terms are important, and examination of Eq. 15 shows that the curvature and normal diffusion terms both scale inversely with the length scale associated with mixture fraction gradients, and so should stay in proportion as Reynolds number changes. Of course, the analysis is conditioned on the extent to which combustion is fast enough to maintain a coherent flame sheet. In recent 3D simulations of a non-premixed temporal ethylene/air jet flame [49], the flame surface colored by  $v_\xi$  is very similar to that presented here: that is, the flame is wrinkled and strained, with positive values of  $v_\xi$  where the flame is negatively curved (and vice versa). Hence, we expect 3D results to be similar to the 2D results of this paper. We noted previously that history effects of the soot growth can mask flame dynamic effects. For example the soot may grow in a region of positive  $v_\xi$ , only to have the flame curvature change sign, without a corresponding immediate change in the soot concentration. The results of the present work will be most relevant for turbulent flows for which the timescales of eddies that wrinkle the flame are similar to timescales of the soot chemistry.

## 6. Conclusions

We have performed a direct numerical simulation of a two-dimensional, unsteady, non-premixed, turbulent ethylene flame with soot formation. This represents the first extension of fully resolved DNS with detailed chemistry and transport to unsteady sooting flames. The purpose of this work has been to examine soot-flame interactions in a multidimensional, unsteady configuration. Several important results are summarized below:

- We have shown that the location of soot relative to a flame, as measured by the mixture fraction, has a strong impact on the local concentrations of soot, the rates of soot reaction, and the soot temperatures.

- Soot spreads over mixture fractions from 0.1 to 0.8 in the 5 ms residence time, with mass fractions ranging from 0-0.22 ( 2 ppmv). This broad spread of soot was shown to result from its differential diffusion.
- Soot transport is governed by fluid convection and thermophoresis. In the present flame, fluid convection dominates soot thermophoresis (by a factor of about 10) and soot is mainly convected with the flow. The flame displacement velocity and fluid convective velocity is of the same order of magnitude in the simulation. The soot-flame position is then given by the relative motion between the flame surface and the fluid motion.
- The flame displacement velocity was computed and we have shown that the soot concentrations peak where the flame displacement velocity is zero or positive—i.e. where the flame moves towards the soot.
- The flame displacement velocity is derived from two terms: a normal diffusion term, present in all flames, and a curvature term present only in multidimensional flames. Both terms are important for the present configuration. Since the stoichiometric mixture fraction is low ( $\xi_{st} = 0.064$ ), normal diffusion generally moves the flame toward the air stream, away from soot. The curvature term augments the flame displacement velocity so that flames curved towards the fuel stream have a flame displacement velocity shifted towards the fuel stream, while the converse occurs for flames curved toward the air stream.
- We also have observed the possibility of low levels of soot-flame breakthrough in regions of high flame curvature.
- While soot mass fraction shows a high degree of scatter in magnitude and mixture fraction, temperature shows very little scatter, and soot reaction rates are sharply located in the mixture fraction coordinate. These observations have been known and used by others in modelling turbulent sooting flames, but the influence of differential soot transport due to multidimensional flame effects should be accounted for to accurately predict flame radiation and soot emission.

## 7. Acknowledgments

This work was supported by the U. S. Department of Energy, Office of Basic Energy Sciences, Division of Chemical Sciences, Geosciences, and Biosciences, and the Air Force Office of Scientific Research. Simulations were performed at Sandia National Laboratories on the Thunderbird Linux Cluster. Sandia National Laboratories is a multiprogram laboratory operated by Sandia Corporation, a Lockheed Martin Company, for the United States Department of Energy under contract DE-AC04-94-AL85000.

## References

- [1] N. Peters, Laminar diffusion flamelet models in non-premixed turbulent combustion, *Prog. Energy Combust. Sci.* 10 (1984) 319–339.
- [2] N. J. Brown, K. L. Revzan, M. Frenklach, Detailed kinetic modelling of soot formation in ethylene-air mixtures reacting in a perfectly stirred reactor, *Proc. Combust. Inst.* 27 (1962) 1573–1580.
- [3] J. Appel, H. Bockhorn, M. Frenklach, Kinetic modelling of soot formation with detailed chemistry and physics: laminar premixed flames of C<sub>2</sub> hydrocarbons, *Combust. Flame* 121 (2000) 122–136.
- [4] K. M. Leung, R. P. Lindstedt, A simplified reaction mechanism for soot formation in nonpremixed flames, *Combust. Flame* 87 (1991) 289–305.
- [5] H. Wang, D. X. Du, C. J. Sung, C. K. Law, Experiments and numerical simulation on soot formation in opposed-jet ethylene diffusion flames, *Proc. Combust. Inst.* 26 (1996) 2359–2368.
- [6] M. D. Smooke, R. J. Hall, M. B. Colket, J. Fielding, M. B. Long, C. S. McEnally, L. D. Pfefferle, Investigation of the transition from lightly sooting towards heavily sooting co-flow ethylene diffusion flames., *Combust. Theor. Model.* 8 (2004) 593–606.
- [7] C. R. Shaddix, T. C. Williams, L. G. Blevins, R. W. Schefer, Flame structure of steady and pulsed sooting inverse jet diffusion flames, *Proc. Combust. Inst.* 30 (2005) 1501–1508.
- [8] M. D. Smooke, C. S. McEnally, L. D. Pfefferle, Computational and experimental study of soot formation in a coflow, laminar diffusion flame, *Combust. Flame* 117 (1999) 117–139.
- [9] C. R. Kaplan, C. R. Shaddix, K. C. Smyth, Computations of enhanced soot production in time-varying CH<sub>4</sub>/air diffusion flames, *Combust. Flame* 106 (1996) 392–405.
- [10] J. Du, R. L. Axelbaum, The effect of flame structure on soot-particle inception in diffusion flames, *Combust. Flame* 100 (1995) 367–375.
- [11] J. Du, R. L. Axelbaum, C. K. Law, The influence of carbon dioxide and oxygen as additives on soot formation in diffusion flames, *Proc. Combust. Inst.* 23 (1990) 1501–1507.
- [12] A. Atreya, C. Zhang, H. K. Kim, T. Shamim, J. Suh, The effect of changes in the flame structure on the formation and destruction of soot and no in radiating diffusion flames, *Proc. Combust. Inst.* 26 (1996) 2181–2189.
- [13] K. C. Lin, G. M. Faeth, Effects of hydrodynamics on soot formation in laminar opposed-jet diffusion flames, *J. Propul. Power* 12 (4) (1996) 691–698.
- [14] B. H. Chao, S. Liu, R. L. Axelbaum, On soot inception in non-premixed flames and the effects of flame structure, *Combust. Sci. Technol.* 138 (1998) 105–135.
- [15] K. T. Kang, J. Y. Hwang, S. H. Chung, Soot zone structure and sooting limit in diffusion flames: comparison of counterflow and coflow flames, *Combust. Flame* 109 (1997) 266–281.
- [16] J. Y. Hwang, S. H. Chung, Growth of soot particles in counterflow diffusion flames of ethylene, *Combust. Flame* 125 (2001) 752–762.
- [17] S. B. Pope, *Turbulent Flows*, Cambridge University Press, New York, 2000.
- [18] C. A. Kennedy, M. H. Carpenter, R. M. Lewis, Low-storage, explicit runge-kutta schemes for the compressible navier-stokes equations, *Appl. Num. Math.* 35 (3) (2000) 177–219.
- [19] C. A. Kennedy, M. H. Carpenter, A comparison of several new numerical methods for the simulation of compressible shear layers, *Appl. Num. Math.* 14 (4) (1994) 397–433.
- [20] R. J. Kee, F. M. Rupley, J. A. Miller, *Chemkin, Reaction Design, Inc.*, San Diego CA (2000).
- [21] Z. Qin, V. V. Lissianski, H. Yang, W. C. Gardiner, S. G. Davis, H. Wang, Combustion chemistry of propane: a case study of detailed reaction mechanism optimization, *Proc. Combust. Inst.* 28 (2000) 1663–1669.
- [22] T. F. Lu, C. K. Law, A directed relation graph method for mechanism reduction, *Proc. Combust. Inst.* 30 (2005) 1333–1341.
- [23] T. F. Lu, C. K. Law, On the applicability of direction relation graph to the reduction of reaction mechanisms, *Combust. Flame* 146 (3) (2006) 472–483.
- [24] X. L. Zheng, T. F. Lu, C. K. Law, Experimental counterflow ignition temperatures and reaction mechanisms of 1,3-butadiene, *Proc. Combust. Inst.* 31 (2007) 367–375.
- [25] T. F. Lu, Y. Ju, C. K. Law, Complex csp for chemistry reduction and analysis, *Combust. Flame* 126 (1-2) (2001) 1445–1455.
- [26] T. F. Lu, C. K. Law, A systematic approach to obtain analytic solution of quasi steady state species in reduced mechanisms, *J. Phys. Chem. A* 110 (49) (2006) 13202–13208.
- [27] H. Pitsch, E. Riesmeier, N. Peters, Unsteady flamelet modelling of soot formation in turbulent diffusion flames, *Combust. Sci. Technol.* 158 (2000) 389–406.
- [28] S. K. Friedlander, *Smoke Dust and Haze: Fundamentals of Aerosol Behavior*, 1st Edition, John Wiley and Sons, New York, 1977.
- [29] Y. Ju, H. Guo, K. Maruta, F. Liu, On the extinction limit and flammability limit of non-adiabatic stretched methane-air premixed flames, *J. Fluid Mech.* 342 (1997) 315–334.
- [30] W. L. Grosshandler, RADCAL: a narrow-band model for radiation calculations in a combustion environment, *NIST Technical Note* 1402 (1993).
- [31] T. Passot, A. Pouquet, Numerical simulation of compressible homogeneous flows in the turbulent regime, *J. Fluid Mech.* 181 (1987) 441–466.
- [32] A. Coppalle, D. Joyeux, Temperature and soot volume fraction in turbulent diffusion flames: measurements of mean and fluctuating values, *Combust. Flame* 96 (1994) 275–285.
- [33] B. Hu, B. Yang, U. O. Koçlu, Soot measurements at the axis of an ethylene/air non-premixed turbulent jet flame, *Combust. Flame* 134 (2003) 93–106.
- [34] R. W. Bilger, S. H. Starner, R. J. Kee, On reduced mechanisms for methane-air combustion in nonpremixed flames, *Combust. Flame* 80 (2) (1990) 135–149.
- [35] C. H. Gibson, Fine structure of scalar fields mixed by turbulence. i. zero-gradient points and minimal gradient surfaces, *Phys. Fluids* 11 (11) (1968) 2305–2315.
- [36] S. B. Pope, The evolution of surfaces in turbulence, *Int. J. Engng. Sci.* 26 (5) (1988) 445–469.
- [37] T. Echehki, J. H. Chen, Analysis of the contribution of curvature to premixed flame propagation, *Combust. Flame* 118 (1999) 308–311.
- [38] N. Peters, *Turbulent Combustion*, Cambridge University Press, Cambridge, United Kingdom, 2000.
- [39] E. Van Kalmouth, D. Veynante, Direct numerical simulations analysis of flame surface density models for nonpremixed combustion, *Phys. Fluids* 10 (9) (1998) 2347.
- [40] W. Kollmann, J. H. Chen, Dynamics of the flame surface area in turbulent non-premixed combustion., *Proc. Combust. Inst.* 25 (1994) 1091–1098.
- [41] H. Guo, F. Liu, G. J. Smallwood, Soot and no formation in counterflow ethylene/oxygen/nitrogen diffusion flames., *Combust. Theor. Model.* 8 (2004) 475–489.
- [42] K. G. Neoh, J. B. Howard, A. F. Sarofim, *Soot oxidation in flames*, Plenum Pub Corp, New York, 1981, pp. 261–282.
- [43] D. Bradley, G. Dixon-Lewis, S. E. Habik, E. M. J. Mushi, The oxidation of graphite powder in flame reaction zone, *Proc. Combust. Inst.* 20 (1984) 931.
- [44] J. Nagle, R. F. Strickland-Constable, Oxidation of carbon between 1000–2000 °C., *Proc. of the 5th Carbon Conference* 1 (1962) 154–164.
- [45] R. O. Fox, *Computational models for turbulent reacting flows*, Cambridge University Press, Cambridge, United Kingdom, 2003.
- [46] A. W. Cook, J. J. Riley, G. Kosaly, A laminar flamelet approach to subgrid-scale chemistry in turbulent flows, *Combust. Flame* 109 (1997) 332–341.
- [47] H. Pitsch, N. Peters, A consistent flamelet formulation for non-premixed combustion considering differential diffusion effects, *Combust. Flame* 114 (1998) 26–40.

- [48] X. S. Bai, M. Balthasar, F. Mauss, L. Fuchs, Detailed soot modeling in turbulent jet diffusion flames, *Proc. Combust. Inst.* 27 (1998) 1623–1630.
- [49] D. O. Lignell, Direct numerical simulation of soot formation in nonpremixed, turbulent ethylene flames, Ph.D. thesis, University of Utah (pending).